Decoding the stellar fossils of the dusty Milky Way progenitors

de Bennassuti, Matteo; Schneider, Raffaella; Valiante, Rosa; Salvadori, Stefania

Published in:
Monthly Notices of the Royal Astronomical Society

DOI:
10.1093/mnras/stu1962

Publication date:
2014

Monthly Notices
of the
ROYAL ASTRONOMICAL SOCIETY

MNRAS **445,** 3039–3054 (2014) doi:10.1093/mnras/stu1962

Decoding the stellar fossils of the dusty Milky Way progenitors

Matteo de Bennassuti,[1,2]★ Raffaella Schneider,[2] Rosa Valiante[2] and Stefania Salvadori[3]

[1]*Dipartimento di Fisica, Sapienza, Università di Roma, Piazzale Aldo Moro 5, I-00185 Roma, Italy*
[2]*INAF–Osservatorio Astronomico di Roma, Via di Frascati 33, I-00040 Monte Porzio Catone, Italy*
[3]*Kapteyn Astronomical Institute, University of Groningen, Landleven 12, NL-9747 AD Groningen, the Netherlands*

Accepted 2014 September 17. Received 2014 August 28; in original form 2014 June 4

ABSTRACT

We investigate the metallicity distribution function (MDF) in the Galactic halo and the relative fraction of carbon-normal and carbon-rich stars. To this aim, we use an improved version of the semi-analytical code GAlaxy MErger Tree and Evolution (GAMETE), that reconstructs the hierarchical merger tree of the Milky Way (MW), following the star formation history and the metal and dust evolution in individual progenitors. The predicted scaling relations between the dust, metal and gas masses for MW progenitors show a good agreement with observational data of local galaxies and of gamma-ray burst (GRB) host galaxies at $0.1 < z < 6.3$. Comparing the simulated and the observed MDF, we find that in order to predict the formation of hyper-iron-poor stars at [Fe/H] < -4, faint supernova (SN) explosions have to dominate the metal yields produced by Population III (Pop III) stars, disfavouring a Pop III initial mass function that extends to stellar masses $>140\,M_{\odot}$, into the Pair-Instability SN progenitor mass range. The relative contribution of C-normal and C-enhanced stars to the MDF and its dependence on [Fe/H] points to a scenario where the Pop III/II transition is driven by dust cooling, and the first low-mass stars form when the dust-to-gas ratio in their parent clouds exceeds a critical value of $\mathcal{D}_{\rm crit} = 4.4 \times 10^{-9}$. Other transition criteria do not predict any C-normal stars below [Fe/H] < -4, at odds with observations.

Key words: stars: formation – stars: Population II – stars: Population III – supernovae: general – Galaxy: evolution – galaxies: evolution – galaxies: ISM.

1 INTRODUCTION

The physical conditions which enable the formation of the first low-mass and long-lived stars in the Universe is still a subject of debate. According to the most recent numerical studies of primordial star formation in the first minihaloes, the final outcome appears to be the formation of a massive stellar binary or of a small multiple of massive stars (for a recent comprehensive review see Bromm 2013). Although this represents a paradigm shift compared to the original 'standard model for the first stars', which presumed the first Population III (Pop III) stars to be very massive and to form in isolation, we are still far from being able to predict the resulting stellar mass spectrum. The best available indications from numerical studies suggest that the first stars formed in a broad mass range, from 10 to 1000 $M_{\odot}$, but that most of them are distributed around a few tens to a few hundred solar masses (Hosokawa et al. 2011; Greif et al. 2012; Turk et al. 2012; Hirano et al. 2014). Occasionally, one of the secondary protostars formed during disc fragmentation is seen to migrate to higher stellar orbit and may eventually form a low-mass primordial star. Yet, no evidence for the existence of such primordial low-mass stars has been found in surveys of the Galactic halo and in nearby dwarfs (Beers & Christlieb 2005; Tolstoy, Hill & Tosi 2009).

Once the first supernovae (SNe) explode and start to seed the gas with metals and dust grains, the physical properties of star-forming regions change, eventually allowing the formation of the first low-mass Pop II stars. Gas at low metallicity can achieve larger cooling rates through additional molecular species (HD, OH, CO, H_2O), fine-structure line cooling (mostly O I and C II), and thermal emission from dust grains (Omukai 2000; Schneider et al. 2002; Omukai et al. 2005). The relative importance of these coolants depends on the density (time) regime during the collapse and on the initial metallicity and dust content of the collapsing core.

Cooling due to line emission affects the thermal evolution of collapsing cores at low-to-intermediate densities: when the total metallicity of the gas is $Z < 10^{-2}\,Z_{\odot}$, molecular cooling dominates at $n < 10^5\,{\rm cm}^{-3}$, with an efficiency which increases with metallicity because of the larger molecular formation rate on the surface of dust grains (Omukai et al. 2005; Schneider et al. 2006, 2012a). For more metal enriched clouds, $Z \geq 10^{-2}\,Z_{\odot}$, O I and C II fine-structure line cooling dominate the thermal evolution at

★ E-mail: matteo.debennassuti@oa-roma.inaf.it

$n < 10^4\,\mathrm{cm}^{-3}$, until the non-local thermodynamic equilibrium–local thermodynamic equilibrium transition occurs and the cooling efficiency decreases. Bromm & Loeb (2003) have derived the critical O and C abundances required to overcome the compressional heating rate and fragment the gas, finding $[\mathrm{C/H}]_{\mathrm{cr}} = -3.5$ and $[\mathrm{O/H}]_{\mathrm{cr}} = -3.05$. Frebel, Johnson & Bromm (2007) have further explored the role of metal fine-structure line cooling by introducing the so-called transition discriminant – a combination of the C and O abundances – that enables the formation of Pop II stars when its value exceeds a critical threshold of $D_{\mathrm{trans,\,cr}} = -3.5 \pm 0.2$. Comparing this theoretical prediction with observations of metal-poor stars in the halo of the Milky Way (MW) and its dwarf satellites, they find that most of the stars have $D_{\mathrm{trans}} > D_{\mathrm{trans,\,cr}}$, with the exception of SDSS J102915+172927, a star with $[\mathrm{Fe/H}] = -4.99$ that falls in the forbidden zone for metal fine-structure line cooling (Caffau et al. 2011b). Note also that given the typical gas temperatures and densities where line-induced fragmentation takes place, the associated Jeans-unstable fragment masses are still relatively large, with masses $\geq 10\,\mathrm{M}_{\odot}$ (Schneider et al. 2006). In a recent numerical simulation, Safranek-Shrader, Milosavljević & Bromm (2014) have confirmed that there is a clear metallicity threshold for widespread fragmentation between (10^{-4}) and $(10^{-3})\,\mathrm{Z}_{\odot}$ in high-redshift, atomic-cooling haloes: fine-structure line cooling allows the gas to cool to the cosmic microwave background (CMB) temperatures and form a cluster of size $\sim$1 pc, with typical fragment masses $\sim$50–100 $\mathrm{M}_{\odot}$, consistent with the Jeans masses expected at the end of the fragmentation phase. Although the simulations do not follow the evolution of the cluster to higher densities, taking these results at face value it appears that fine-structure line cooling is not capable of producing solar-mass fragments that have the potential to survive until the present day, corroborating previous findings based on semi-analytical models (Schneider et al. 2006).

A pervasive fragmentation mode that allows the formation of solar or subsolar-mass fragments is activated at higher gas densities, $n > 10^{10}$–$10^{12}\,\mathrm{cm}^{-3}$, when dust grains are collisionally excited and emit continuum radiation, thereby decreasing the gas temperature until it becomes thermally coupled with the dust temperature $T = T_{\mathrm{dust}}$ or the gas becomes optically thick (Schneider et al. 2002). The efficiency of this physical process depends on the dust-to-gas ratio and on the total grain cross-section, with smaller grains providing a larger contribution to cooling (Schneider et al. 2006). Hence, the minimal conditions for dust-induced fragmentation have been expressed in terms of a minimal critical dust-to-gas ratio,

$$S\mathcal{D}_{\mathrm{cr}} = 1.4 \times 10^{-3}\,\mathrm{cm}^2\,g^{-1} \left(\frac{T}{10^3\,\mathrm{K}}\right)^{-1/2} \left(\frac{n}{10^{12}\,\mathrm{cm}^{-3}}\right)^{-1/2}, \quad (1)$$

where S is the total cross-section of dust grains per unit dust mass and the expression holds in the regime where dust cooling is effective, hence $T_{\mathrm{dust}} \ll T$. An extensive parameter-space exploration shows that $\mathcal{D}_{\mathrm{cr}} \sim 4.4 \times 10^{-9}$ can be considered as a good representative value for the minimal dust enrichment required to activate dust-induced fragmentation (Schneider et al. 2012a). These results have been confirmed by numerical simulations (Tsuribe & Omukai 2006, 2008; Clark, Glover & Klessen 2008; Omukai, Hosokawa & Yoshida 2010; Dopcke et al. 2011). In addition, the observed properties of SDSS J102915+172927 provide a strong indication that low-mass star formation may have occurred in the absence of efficient metal-line cooling, supporting a dust-driven transition (Chiaki et al. 2014; Schneider et al. 2014).

It is clear from the above considerations that stellar archaeology of the most metal-poor stars represents a promising way to explore the first phases of star formation and metal enrichment in the Universe, constraining the conditions for the formation of the first low-mass stars. In particular, the low-metallicity tail of the metallicity distribution function (MDF, i.e. the number distribution of stars as function of their [Fe/H][1]) at $[\mathrm{Fe/H}] < -2$ and the observed surface elemental abundances of the most metal-poor stars can provide important observational constraints on the nature of Pop III stars and on the formation efficiency of the first Pop II stars (Karlsson 2006; Tumlinson 2006; Salvadori, Schneider & Ferrara 2007; Salvadori, Ferrara & Schneider 2008; Komiya et al. 2009; Salvadori & Ferrara 2009; Salvadori et al. 2010; Komiya 2011). A large sample of stars in the MW halo and its satellites has been collected by the HK survey (Beers, Preston & Shectman 1992), by the Hamburg/ESO survey (HES; Wisotzki et al. 2000; Christlieb 2003), by the Sloan Digital Sky Survey (SDSS; York et al. 2000; Gunn et al. 2006) and by the Sloan Extension for Galactic Understanding and Exploration (Yanny et al. 2009). Many studies have been performed on these data sets, to assess their completeness (Christlieb et al. 2008, Schörck et al. 2009), to study the carbon-enhancement degree (Carollo et al. 2012; Norris et al. 2013; Spite et al. 2013; Yong et al. 2013b) and the chemical abundances of metal-poor stars (see the reviews of Beers & Christlieb 2005; Frebel & Norris 2013; Karlsson, Bromm & Bland-Hawthorn 2013, and references therein). These observations show that the MDF suddenly drops at $[\mathrm{Fe/H}] \approx -4$ so that only five stars are observed at $[\mathrm{Fe/H}] \lesssim -4.75$, among which the recently discovered SMSS J031300.36−670839.3 (hereafter SMSS J031300) with $[\mathrm{Fe/H}] < -7.1$ (Keller et al. 2014). In general, metal-poor stars in the MW halo have a well-defined abundance pattern at $[\mathrm{Fe/H}] < -2.5$ (Cayrel et al. 2004), that is compatible with theoretical yields of Pop III core-collapse (cc) SNe with progenitor masses in the range 10–100 $\mathrm{M}_{\odot}$ (Heger & Woosley 2010; Limongi & Chieffi 2012). Yet, there is a class of stars, the so-called carbon-enhanced extremely metal-poor stars (CEMP, defined as those with $[\mathrm{C/Fe}] > +1$; Beers & Christlieb 2005), whose fraction grows with decreasing [Fe/H], being (10–20) per cent at $[\mathrm{Fe/H}] < -2$ (Yong et al. 2013b) and reaching 80 per cent at $[\mathrm{Fe/H}] < -4.75$. The origin of CEMP stars is still debated and many alternative explanations have been proposed (see Norris et al. 2013 for a recent critical assessment of the possible formation pathways).

In this paper, we describe an improved version of the hierarchical semi-analytical code GAlaxy MErger Tree and Evolution (GAMETE) originally developed by Salvadori et al. (2007). Our main goal is to investigate whether current observations of the MDF and of the relative contribution of CEMP stars at different [Fe/H] can provide constraints on the initial mass function (IMF) of Pop III stars and on the physics governing the Pop III/II transition. To this aim, following Valiante et al. (2011), we have developed a chemical evolution model with dust in a two-phase interstellar medium (ISM); in this model, grains are destroyed by SN shocks in the diffuse, hot phase, but are shielded from destruction in the dense, cold phase, where they can grow in mass by accreting gas-phase metals. Using this model, we can predict the stellar, gas, metal and dust content of all the MW progenitors along the simulated merger trees from $z = 20$ down to $z = 0$. With the aim of constraining the model free parameters, we compare the theoretical predictions with observations of the global properties of the MW, such as the gas mass, the stellar content, the metallicity, and the dust-to-gas ratio. In addition, we show that the properties of the MW progenitors

[1] $[\mathrm{X/Y}] = \log_{10}(N_X/N_Y) - \log_{10}(N_X/N_Y)_{\odot}$, for elements X and Y. We adopt solar abundances from Caffau et al. (2011a).

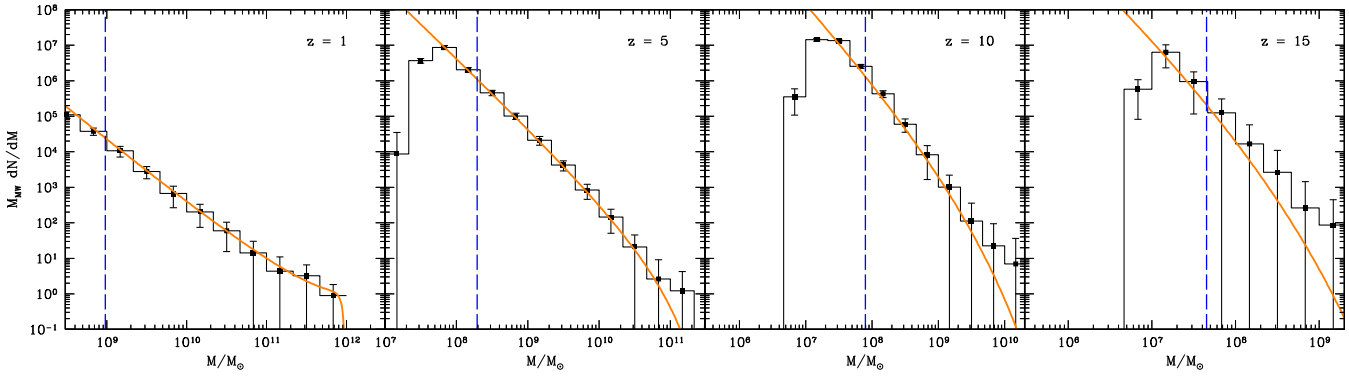

Figure 1. Number of haloes as function of halo mass at different redshifts ($z = 1$, 5, 10, 15 from left to right) for a MW-like final DM halo of 10^{12} $M_{\odot}$. The orange solid lines are the analytic predictions from the EPS theory, while the histograms are the simulated mass functions averaged over 50 merger trees. Error bars are given by Poissonian errors. The vertical lines correspond to the adopted minimum mass of star-forming haloes, $M_{\rm sf}$, at the corresponding redshift.

predicted by the model appear to be in good agreement with the observed scaling relations between the dust/metal and gas/stellar components inferred from samples of galaxies at $0 < z < 6$.

The paper is organized as follows: in Section 2, we give a short description of the basic properties of the GAMETE code, with particular attention to the new features implemented in this work. In Section 3, we explain how we calibrate the model free parameters to reproduce the observed global properties of the MW. In Section 4, we compare the predicted properties of MW progenitors with observational data collected from various galaxy samples. In Section 5, we apply the model to Galactic archaeology, exploring the dependence of the simulated MDF to the assumed Pop III IMF (Section 5.1) and Pop III/II transition criteria (Section 5.2); we make specific predictions for the metallicity distribution of CEMP stars (Section 5.3), comparing the model with observations. Finally, in Section 6, we discuss our results and present our main conclusions in Section 7.

2 DESCRIPTION OF THE MODEL

The GAMETE code allows us to reproduce the observed global properties of the MW, such as the mass of gas and stars, metallicity and dust-to-gas ratio, predicting their evolution along cosmic time. Enrichment processes are assumed to be regulated by stars, both asymptotic giant branch (AGB) stars and SNe, which eject metals and dust into the ISM according to their stellar lifetime (i.e. stars with different masses and metallicities evolve on different time-scales); at each time, the star formation rate (SFR) is taken to be proportional to the available mass of gas in the ISM, $\mathrm{SFR}(t) = \epsilon_* M_{\rm ISM}(t)/t_{\rm dyn}(t)$, where $t_{\rm dyn}(t)$ is the dynamical time-scale of the host dark matter (DM) halo, and ϵ_* is the star formation efficiency, a free parameter of the model.

We follow the formation and evolution of a MW-like galaxy in the framework of the Lambda cold dark matter model. Cosmological parameters are taken from the recent results of the Planck Collaboration XVI (2014): $h_0 = 0.67$; $\Omega_{\rm b} h^2 = 0.022$; $\Omega_{\rm m} = 0.32$; $\Omega_{\Lambda} = 0.68$; $\sigma_8 = 0.83$; and $n_{\rm s} = 0.96$. Galaxies are assembled via galaxy–galaxy mergers and/or mass accretion. The hierarchical merger histories (merger trees) of the DM haloes are reconstructed using a binary Monte Carlo algorithm based on the Extended Press and Schechter (EPS; Press & Schechter 1974) theory. Here, we briefly summarize the main features of this method and refer the reader to Salvadori et al. (2007, 2008) for further details. The code traces the merger tree backward in time, starting from a MW-like DM halo of $M_{\rm MW} = 10^{12}$ $M_{\odot}$ at redshift $z = 0$ (Binney & Merrifield 1998; Klypin, Zhao & Somerville 2002) up to $z \sim 20$. At each redshift, DM haloes can either fragment in two smaller haloes, called *progenitors* and/or loose mass. DM progenitors are identified as haloes with masses larger than the so-called resolution mass, $M_{\rm res}$. It is customary in merger-tree models to define the mass below $M_{\rm res}$ that is not part of collapsed objects as the external or Galactic medium (GM). This is the environment out of which haloes virialize. The free parameters which describe the merger-tree model are the redshift interval (dz) and the resolution mass, which are chosen in order to ensure the binarity of the code and the agreement between the resulting mass function of progenitor haloes and the theoretically predicted EPS distribution over the relevant redshift range.

We also assume that star formation in minihaloes is suppressed by strong radiative feedback effects (Ciardi & Ferrara 2005). Hence, star formation occurs in haloes above a minimum mass, $M_{\rm sf}$, that corresponds to the minimum mass of Lyα cooling haloes, hence to haloes with virial temperature $T_{\rm vir} = 2 \times 10^4$ K, $M_{\rm sf}(z) = M_{\rm vir}(2 \times 10^4\,\mathrm{K}, z)$ (Barkana & Loeb 2001). To properly sample the low-mass end of the simulated progenitor mass function, we adopt a resolution mass of $M_{\rm res}(z) = M_{\rm sf}(z)/10$. Fig. 1 shows the comparison between the theoretical EPS DM halo mass function and the simulated one averaged over 50 merger trees. Different panels correspond to different redshifts and in each panel the vertical line represents the $M_{\rm sf}(z)$ computed at the corresponding redshift. The comparison shows that there is a good agreement with the EPS (within the error bars), particularly for $M \gtrsim M_{\rm sf}(z)$, which is the mass range we are interested in.

An increase in the minimum mass of star-forming haloes is expected during cosmic reionization, due to the increased Jeans mass in ionized regions, which causes the quenching of the gas infall in haloes below a given circular velocity $v_{\rm c}(z)$ or DM halo mass (Gnedin 2000; Hoeft et al. 2006; Okamoto, Gao & Theuns 2008). While the details of the evolution of $v_{\rm c}(z)$ depend on the reionization redshift, amplitude of the ionizing background and redshift (Noh & McQuinn 2014), here we simply assume that star formation is quenched in DM haloes with circular velocities smaller than $v_{\rm c} = 30\,\mathrm{km\,s^{-1}}$ when $z < z_{\rm reion} = 6$ (Salvadori & Ferrara 2009).

2.1 Two-phase model for the ISM

We have further implemented GAMETE to describe the evolution of the gas in two separate phases of the ISM: a *diffuse* component

(warm/hot low-density gas), where dust can be destroyed by SN shocks, and a *dense* or *molecular cloud* (MC) component (cold and dense gas), where star formation occurs and where dust grains can grow in mass by accreting gas-phase metals being shielded from destructive processes. While grain reprocessing in the ISM is still subject to many uncertainties, observations indicate that dust destruction takes place in regions of the ISM shocked to velocities of the order of 50–200 km s^{-1} (Welty et al. 2002; Podio et al. 2006; Slavin 2009). In our model, part of the newly formed dust in SNe is destroyed *in situ* (hence in the cold dense medium) by the SN reverse shock (Bianchi & Schneider 2007). Note also that in the dense phase of the ISM, the grains can grow to larger sizes and hence are generally more resistant to sputtering.

For each quantity (gas, metals, dust), the total mass is simply given by the sum of the masses in the two components. The gas present in the MW environment or GM, where haloes are embedded, is assumed to be only in the diffuse phase; when a DM halo first virializes, the ISM is initially accreted in the diffuse phase, with a gas infall rate $\dot{M}_{\rm inf}$ (Salvadori et al. 2008). For star-forming systems, with $M_{\rm halo} \geq M_{\rm sf}$, the following processes are considered:

(i) the diffuse gas, $M_{\rm ISM}^{\rm diff}$, condenses into the dense molecular phase, $M_{\rm ISM}^{MC}$, at a rate $\dot{M}_{\rm cond}$;
(ii) stars (M_*) form out of dense gas with an SFR;
(iii) stars evolve and return gas, metals and dust in the diffuse phase;
(iv) dust in MCs accretes gas-phase metals, while dust in the diffuse phase is partly destroyed by interstellar shocks due to SN explosions;
(v) mechanical feedback due to SN explosions drives gas outflows, ejecting the diffuse gas into the GM;
(vi) part of the dense phase returns to the diffuse phase due to dispersion of MCs.

As a result, the time evolution of the gas is described by the following set of differential equations:

$$\dot{M}_{\rm ISM}^{\rm diff}(t) = \dot{M}_{\rm inf}(t) - \dot{M}_{\rm cond}(t) + \dot{R}(t) - \dot{M}_{\rm ej}^{\rm diff}(t), \quad (2)$$

and

$$\dot{M}_{\rm ISM}^{\rm MC}(t) = \dot{M}_{\rm cond}(t) - {\rm SFR}(t) - \dot{M}_{\rm ej}^{\rm MC}(t). \quad (3)$$

In the above expressions, $\dot{R}(t)$ is the gas returned by stars to the ISM (Salvadori et al. 2008), and $\dot{M}_{\rm ej}^{\rm diff}(t)$ and $\dot{M}_{\rm ej}^{\rm MC}(t)$ represent the diffuse and dense gas ejection rate. The total mass of gas ejected per unit time $\dot{M}_{\rm ej}$ due to SN-driven mechanical feedback is proportional to the SN explosion rate and the wind energy is regulated by a free parameter $\epsilon_{\rm w}$, controlling the conversion efficiency of SN explosion energy into kinetic energy (see equation 9 of Salvadori et al. 2008). Since the effect of SN driven on different ISM phases is still poorly understood (Efstathiou 2000; Powell, Slyz & Devriendt 2011), we studied different mass-loading prescriptions, finding that the higher is the MC ejection rate, the higher must be the condensation rate to reproduce the global properties of the MW. Hence, we decide to follow Fu et al. (2013) and consider that the energy injected into the medium from SNe leads to the ejection only of the hot diffuse phase through mechanical feedback (i.e. $\dot{M}_{\rm ej}^{\rm MC}(t) = 0$).

The physical processes leading to the formation of MCs are still not fully understood (see Dobbs et al. 2013 for a recent review). Here, we adopt a simple empirical description, tailored to reproduce the observed mass of gas in the molecular and atomic components of the MW.

We assume the condensation rate to be proportional to the SFR, hence $\dot{M}_{\rm cond}(t) = \alpha_{\rm MC}\,{\rm SFR}(t)$, where $\alpha_{\rm MC}$ is a free parameter of the model. The above condensation rate is the net result of the mass exchange between the two ISM phases, which is regulated by the condensation of the diffuse gas into MCs,

$$M_{\rm ISM}^{\rm diff}(t)/t_{\rm form} = \frac{1}{1-f}\,\alpha_{\rm MC}\,{\rm SFR}(t), \quad (4)$$

and the dispersal of molecular gas into the diffuse phase,

$$M_{\rm ISM}^{\rm MC}(t)/t_{\rm des} = \frac{f}{1-f}\,\alpha_{\rm MC}\,{\rm SFR}(t), \quad (5)$$

where $0 < f < 1$. Hence, the two-phase structure of the ISM is regulated by the free parameters f and $\alpha_{\rm MC}$. When $f \to 0$, the condensation process is very efficient and the gas content in the ISM is dominated by the MC phase. Conversely, when $f \to 1$ the condensation and dispersal rates are in equilibrium. As a result, the newly condensed phase is rapidly dispersed in the ISM, preventing the formation of a stable dense phase. As we will show in Section 3, the values of the two parameters, $\alpha_{\rm MC}$ and f, have been selected to reproduce the observed molecular and atomic gas masses in the MW.

This two-phase model has been recently applied to high-redshift quasars (Valiante et al. 2014), where accretion on to the central black hole and active galactic nuclei feedback are also included.

2.2 Chemical evolution

The enrichment in heavy elements (including both gas-phase metals and metals locked in dust grains) is described in the two-phase ISM by means of the following equations:

$$\dot{M}_{\rm Z}^{\rm diff}(t) = Z_{\rm vir}(t)\,\dot{M}_{\rm inf}(t) - Z_{\rm diff}(t)\,M_{\rm ISM}^{\rm diff}(t)/t_{\rm form} + Z_{\rm MC}(t)\,M_{\rm ISM}^{\rm MC}(t)/t_{\rm des} + \dot{Y}_{\rm Z}(t) - Z_{\rm diff}(t)\,\dot{M}_{\rm ej}^{\rm diff}(t), \quad (6)$$

and

$$\dot{M}_{\rm Z}^{\rm MC}(t) = Z_{\rm diff}(t)\,M_{\rm ISM}^{\rm diff}(t)/t_{\rm form} - Z_{\rm MC}(t)\,M_{\rm ISM}^{\rm MC}(t)/t_{\rm des} - Z_{\rm MC}(t)\,{\rm SFR}(t) - Z_{\rm MC}(t)\,\dot{M}_{\rm ej}^{\rm MC}(t), \quad (7)$$

where $Z_{\rm diff} = M_Z^{\rm diff}(t)/M_{\rm ISM}^{\rm diff}(t)$ and $Z_{\rm MC} = M_Z^{\rm MC}(t)/M_{\rm ISM}^{\rm MC}(t)$ are the total (gas phase + dust) metallicities of the diffuse and dense phases, $Z_{\rm vir}$ is the metallicity of the gas accreted from the GM and $\dot{Y}_Z(t)$ is the rate at which heavy elements produced by stars are returned to the ISM, given by

$$\dot{Y}_{\rm Z}(t) = \int_{m_*(t)}^{m_{\rm up}} m_Z(m, Z)\,\Phi(m)\,{\rm SFR}(t - \tau_{\rm m})\,{\rm d}m, \quad (8)$$

where the lower limit of integration refers to the mass of a star with a lifetime $\tau_{\rm m} = t$, $m_{\rm Z}(m, Z)$ is the total mass of metals (pre-existing and newly synthesized) produced by a star of initial mass m and metallicity Z, $\Phi(m)$ is the stellar IMF and $m_{\rm up}$ is the upper mass limit of the IMF.

The chemical network has been extended to implement the evolution of dust (Valiante et al. 2009, 2011). In the two-phase ISM, this is described as

$$\dot{M}_{\rm d}^{\rm diff}(t) = \mathcal{D}_{\rm vir}(t)\dot{M}_{\rm inf}(t) - \mathcal{D}_{\rm diff}(t)\,M_{\rm ISM}^{\rm diff}(t)/t_{\rm form} - M_{\rm d}^{\rm diff}(t)/\tau_{\rm d} + \mathcal{D}_{\rm MC}(t)\,M_{\rm ISM}^{\rm MC}(t)/t_{\rm des} + \dot{Y}_{\rm d}(t) - \mathcal{D}_{\rm diff}(t)\dot{M}_{\rm ej}^{\rm diff}(t), \quad (9)$$

and

$$\dot{M}_{\rm d}^{\rm MC}(t) = \mathcal{D}_{\rm diff}(t)\,M_{\rm ISM}^{\rm diff}(t)/t_{\rm form} - \mathcal{D}_{\rm MC}(t)\,M_{\rm ISM}^{\rm MC}(t)/t_{\rm des} - \mathcal{D}_{\rm MC}(t){\rm SFR}(t) + M_{\rm d}^{\rm MC}/\tau_{\rm acc} - \mathcal{D}_{\rm MC}(t)\dot{M}_{\rm ej}^{\rm MC}(t), \quad (10)$$

where $\mathcal{D}_{\rm diff}(t) = M_{\rm d}^{\rm diff}(t)/M_{\rm ISM}^{\rm diff}(t)$ and $\mathcal{D}_{\rm MC}(t) = M_{\rm d}^{\rm MC}(t)/M_{\rm ISM}^{\rm MC}(t)$ are the dust-to-gas (mass) ratios in the two phases, $\mathcal{D}_{\rm vir}$ is the dust-to-gas ratio of the infalling gas and $\dot{Y}_{\rm d}$ is the rate at which dust produced by stars is injected into the ISM by AGB stars and SN explosions (Valiante et al. 2009)

$$\dot{Y}_{\rm d}(t) = \int_{m_*(t)}^{m_{\rm up}} m_{\rm d}(m, Z)\, \Phi(m)\, {\rm SFR}(t - \tau_{\rm m})\, {\rm d}m \tag{11}$$

where $m_{\rm d}(m, Z)$ is the mass of dust produced by a star with mass m and metallicity Z, and all other quantities are the same as in equation (8).

For any given element/grain species i, the corresponding yield is computed as in equations (8) and (11) substituting m_Z and $m_{\rm d}$ with $m_i(m, Z)$. A presentation of the mass- and metallicity-dependent dust and metal yields will be given in Sections 2.3 and 2.5.

Grain growth through accretion of gas-phase metals can occur only in the dense phase of the ISM (see equation 10); following Asano et al. (2013), we model the dust accretion time-scale $\tau_{\rm acc}$ as

$$\tau_{\rm acc} \approx 20\,{\rm Myr} \times \left(\frac{\bar{a}}{0.1\,\mu{\rm m}}\right)\left(\frac{n}{100\ {\rm cm}^{-3}}\right)^{-1}\left(\frac{T}{50\,{\rm K}}\right)^{-3/2}\left(\frac{Z}{{\rm Z}_\odot}\right)^{-1}, \tag{12}$$

where $\bar{a}$ is the typical size of dust grains, n is the number density of the gas in the MC phase, T and Z are the temperature and the gas-phase metallicity of the cloud, respectively. Here, we assume that in the MC phase $n = 10^3$ cm^{-3} and $T = 50$ K, so that the accretion time-scale from a gas at solar metallicity is 2 Myr (Asano et al. 2013).

The destruction time-scale, $\tau_{\rm d}$, is the lifetime of dust grains destroyed by thermal sputtering in high-velocity ($v > 150\,{\rm km\,s^{-1}}$) SN shocks. We assume that dust grains can be destroyed only in the hot diffuse phase of the ISM and that

$$\tau_{\rm d} = \frac{M_{\rm ISM}^{\rm diff}}{\epsilon_{\rm d}\, M_{\rm swept}\, R'_{\rm SN}}, \tag{13}$$

where $\epsilon_{\rm d}$ is the destruction efficiency, $M_{\rm swept}$ is the effective ISM mass that is completely cleared of dust by a single SN shock and $R'_{\rm SN} = f_{\rm SN} R_{\rm SN}$ is the effective SN rate for grains destruction, accounting for the possibility that not all the SNe which interact with the ISM are equally efficient at destroying dust (Dwek & Scalo 1980; McKee 1989; Tielens 2005). In what follows, we assume that stars with masses in the range [140–260] M$_\odot$ explode as Pair-Instability SuperNovae (PISNe; Heger & Woosley 2002). These are very efficient at destroying dust (Nozawa, Kozasa & Habe 2006), hence $f_{\rm PISN} = 1$. Conversely, stars with masses in the range [8–40] M$_\odot$ explode as cc SNe (either faint or ordinary SNe, see Section 2.3) and are less efficient at destroying dust, $f_{\rm SN} = 0.15$. The mass $M_{\rm swept}$ can be computed using the Sedov–Taylor solution for an expanding SN in a homogeneous medium with shock velocity $v_{\rm sh}$ (McKee 1989),

$$M_{\rm swept} = 6800\,{\rm M}_\odot \frac{\langle E_{\rm SN}\rangle/10^{51}\,{\rm erg}}{(v_{\rm sh}/100\,{\rm km\,s^{-1}})^2}, \tag{14}$$

where $v_{\rm sh} \sim 200\,{\rm km\,s^{-1}}$ is the (minimum) non-radiative shock velocity and $\langle E_{\rm SN}\rangle$ is the average SN explosion energy, assumed to be 2.7×10^{52} erg for PISNe and 1.2×10^{51} erg for cc SNe. We adopt the dust destruction efficiencies from Nozawa et al. (2006) for PISNe and from Jones, Tielens & Hollenbach (1996) for SNe, $\epsilon_{\rm d} \sim 0.6$ and $\epsilon_{\rm d} \sim 0.48$, respectively, and assume a reference ISM density of $n_{\rm ISM} = 1$ cm^{-3}.

Note that the mass of gas-phase metals can be easily inferred as $M_Z - M_{\rm d}$.

2.3 Population III stars

We assume Pop III stars to form according to a Larson-type IMF (Larson 1998)

$$\Phi(m) = \frac{{\rm d}N}{{\rm d}m} \propto m^{\alpha-1}{\rm exp}\left(-\frac{m_{\rm ch}}{m}\right) \tag{15}$$

with $\alpha = -1.35$. The value of $m_{\rm ch}$ is chosen in order to have an average mass of Pop III stars of $\sim$40 M$_\odot$ (Hosokawa & Omukai 2009). In the first model that we explore, Pop III stars are assumed to form with masses in the range [10–300] M$_\odot$ with a characteristic mass of $m_{\rm ch} = 20$ M$_\odot$. The corresponding Pop III IMF is shown in the upper-left panel of Fig. 2. We follow the gradual enrichment of the ISM by Pop III stars taking into account their mass-dependent lifetimes (Raiteri, Villata & Navarro 1996; Schaerer 2002), and consider metal and dust yields from cc SNe ($10\,{\rm M}_\odot < m_* < 40\,{\rm M}_\odot$) and PISNe ($140\,{\rm M}_\odot < m_* < 260\,{\rm M}_\odot$); outside these two mass ranges stars are assumed to directly collapse to black hole without ejecting the products of their nucleosynthesis. For the purpose of the present study, we follow the evolution of the total mass in metals with the separate contributions of Fe, C and O using the yields of Woosley & Weaver (1995) for cc SN and of Heger & Woosley (2002) for PISN. In addition, we also follow the enrichment in dust grains produced in the ejecta of Pop III SNe, using the results by Bianchi & Schneider (2007) for cc SNe and by Schneider, Ferrara & Salvaterra (2004) for PISNe. We take into account the partial destruction of the newly formed grains by a reverse shock of moderate intensity (Bianchi & Schneider 2007), so that approximately 7 per cent of the newly condensed dust mass is able to survive and enrich the ISM (Valiante et al. 2009). In the bottom-left panel of Fig. 2, we show the Pop III IMF-integrated yields given by equations (8) and (11) as a function of the minimum stellar mass, $m_*(t)$. Here all the stars are assumed to form in a burst and the total mass ejected is normalized to the total mass of stars formed. In the second Pop III model that we explore, we keep the same Pop III IMF and mass range as described above but we assume that stars in the $10\,{\rm M}_\odot < m_* < 40\,{\rm M}_\odot$ mass range explode as faint SNe, hence are characterized by moderate mixing and strong fallback (Umeda & Nomoto 2003). For these explosions, we adopt metal and dust yields recently computed by Marassi et al. (2014) and show the corresponding IMF and IMF-integrated yields in the central panels of Fig. 2. It is clear from the figure that there are only minor differences between faint and ordinary cc SNe, since massive PISNe are the first to explode and dominate the yields. Only C shows a larger variation, but the difference between the two models is smaller than a factor of $\sim$2. Finally, in the last model that we explore, Pop III stars are assumed to form in the mass range [10–140] M$_\odot$ with a characteristic mass $m_{\rm ch} = 32$ M$_\odot$ (top-right panel), excluding the PISN mass range and assuming faint SNe at $m < 40$ M$_\odot$. The resulting IMF-integrated yields are shown in the bottom-right panel: for stars with $40\,{\rm M}_\odot < m < 140\,{\rm M}_\odot$ the ejected material completely fallbacks on to the star. Hence, stars contribute to the integrated yields only if $m < 40$ M$_\odot$. While metals/dust/C yields are a factor of $\sim$5/20/50 smaller than faint SNe + PISNe case (middle panel), the main feature of faint SNe is the dramatically lower Fe yield (approximately five orders of magnitude smaller). A summary of the three Pop III models that we consider is given in Table 3.

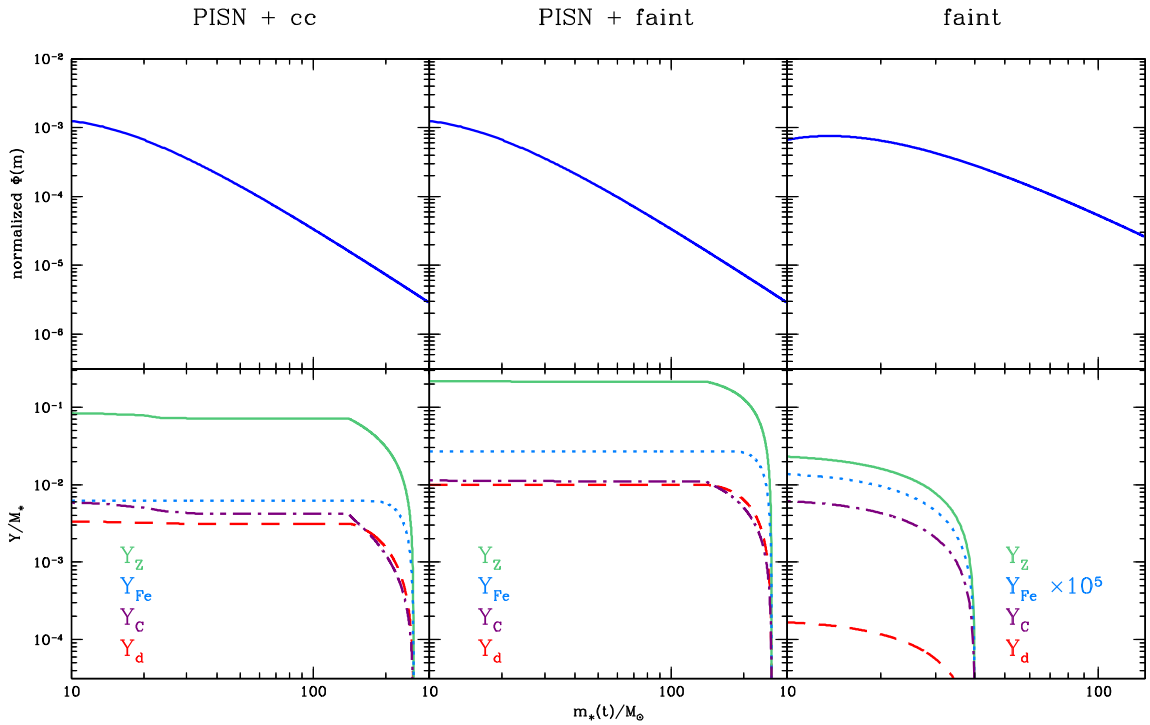

Figure 2. Description of the Pop III models explored. In the upper panels, we show the normalized Pop III IMF that we consider and in the bottom panel the corresponding IMF-integrated yields. These are normalized to the stellar mass formed in a single burst and plotted as a function of the minimum stellar mass (see equations 8 and 11). We show the separate evolution of the total metal (green, solid) and dust (red, dashed) yields and the evolution of the iron (azure, dotted) and carbon (purple, dot–dashed) yields. Left-hand panels: stars form in the mass range [10–300] $M_\odot$ assuming cc-SNe yields for masses $m < 40\,M_\odot$. Middle panels: stars form in the same mass range but faint SNe yields are considered if $m < 40\,M_\odot$. Right-hand panels: stars form in the mass range [10–140] $M_\odot$, excluding the PISN mass range and considering faint SNe yields. Note that in this last case the iron yield is multiplied by a factor of 10^5.

2.4 The Pop III/II transition

As we have discussed in Section 1, one of the goal of the present study is to investigate the potential of current observations of metal-poor stars in the MW halo to constrain the physical conditions that enable the formation of the first low-mass Pop II stars. The chemical evolution model described above allows us to follow the evolution of the mass of gas-phase metals, dust grains, as well as the separate abundances of C, O and Fe in the two-phase ISM. Hence, it enables us to investigate the model predictions assuming different Pop III/II transition criteria. In particular:

(i) *critical metallicity*: low-mass Pop II stars can form when the gas-phase metallicity of MC is larger than $Z_{\rm cr} = 10^{-3.8}\ Z_\odot$ (Bromm et al. 2001);

(ii) *critical dust-to-gas ratio*: Pop II stars form when the dust-to-gas mass ratio of MC is larger than $\mathcal{D}_{\rm cr} = 4.4^{+1.9}_{-1.8} \times 10^{-9}$, where the error bars take into account the modulation due to grain properties (Schneider et al. 2012a); and

(iii) *transition discriminant*: Pop II stars form if the transition discriminant, $D_{\rm trans} = \log_{10}(10^{\rm [C/H]} + 0.9 \times 10^{\rm [O/H]})$, where [C/H] and [O/H] are the total (gas phase + dust) C and O abundance in the MC, is larger than $D_{\rm trans,\,cr} = -3.5 \pm 0.2$ (Frebel & Norris 2013).

Table 3 lists the models that we have explored using different Pop III/II transition criteria.

2.5 Population II stars

Once the criteria for low-mass star formation are met, Pop II stars are assumed to form according to a Larson IMF in the mass range [0.1–100] $M_\odot$ with $m_{\rm ch} = 0.35\,M_\odot$ (Larson 1998) and we consider their evolution taking into account the mass- and metallicity-dependent stellar lifetimes (Raiteri et al. 1996). For stars with $m_* < 8\,M_\odot$, we adopt metal yields from Van den Hoek & Groenewegen (1997) and dust yields for intermediate-mass stars on the AGB phase of the evolution by Zhukovska, Gail & Trieloff (2008). Metal and dust yields for massive stars ($12\,M_\odot < m_* < 40\,M_\odot$) have been taken from Woosley & Weaver (1995) and from Bianchi & Schneider (2007), using the proper mass- and metallicity-dependent values. For stars in the mass range $8\,M_\odot < m_* < 12\,M_\odot$, we interpolate between the AGB yields for the largest-mass progenitor and SN yields for the lowest-mass progenitor. Above 40 $M_\odot$, stars are assumed to collapse to black hole without contributing to the enrichment of the ISM. The chosen IMF and the resulting Pop II IMF-integrated yields are shown in Fig. 3 (upper and lower panels, respectively). The shaded areas represent how yields vary for different stellar progenitor metallicities (see also Valiante et al. 2009). Similarly to what has been assumed for Pop III dust yields, we take into account the partial destruction by the reverse shock of the newly formed dust in SN ejecta; with this choice, the resulting SN dust masses appear to be in good agreement with available observational data of SNe and SN remnants (Schneider et al. 2014; Valiante & Schneider 2014).

3 THE GLOBAL PROPERTIES OF THE MILKY WAY

Since the contribution of Pop III stars to the total SFR is only relevant at high redshifts, the model predictions for global MW properties and for its progenitors are fairly independent of the adopted Pop III IMF and Pop III/II transition criteria. Fig. 4 shows the result

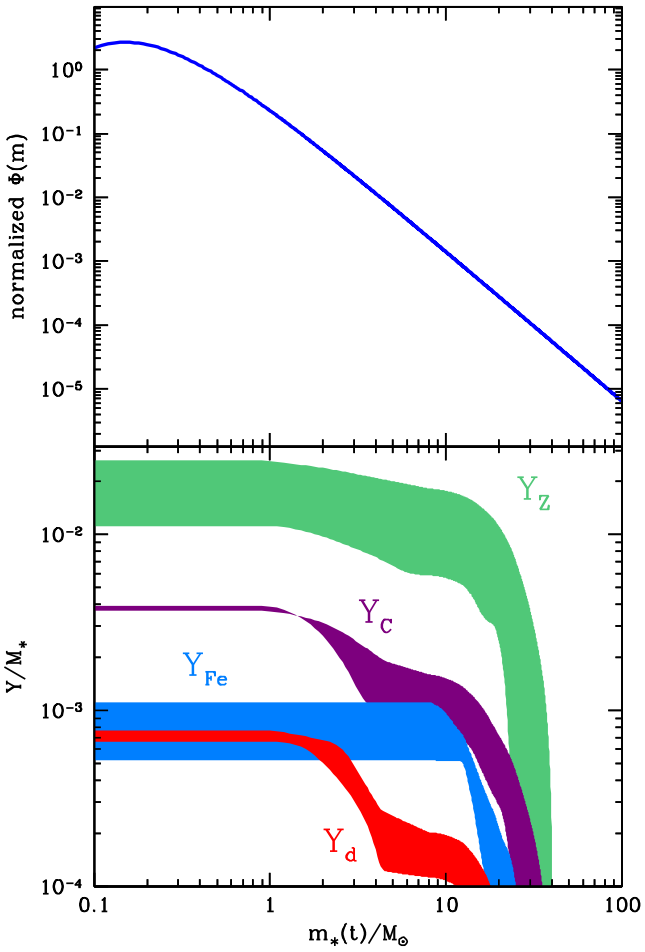

Figure 3. Same as Fig. 2 but for Pop II stars. Shaded areas account for metallicity-dependent yields, with $10^{-4}\,Z_{\odot} < Z < Z_{\odot}$ (see the text).

obtained for a model where the Pop III/II transition occurs when the dust-to-gas ratio in the dense phase of the ISM exceeds the critical value of $\mathcal{D}_{\rm cr} = 4.4 \times 10^{-9}$ and Pop III stars form according to a Larson IMF with masses in the range 10–140 $M_{\odot}$ (model f in Table 3). Hereafter we refer to this model as our reference model. It is clear that metal and dust enrichment prevents Pop III stars from forming at $z < 12$ and that the star formation history is completely dominated by Pop II stars, with a final SFR in good agreement with the observed value.

The model presented in the previous section relies on a number of free parameters, such as the star formation efficiency, ϵ_{*}, the SN-driven wind efficiency $\epsilon_{\rm w}$, and the parameters f and $\alpha_{\rm MC}$ that control the two-phase structure of the ISM. In addition, we have to define the typical density and temperature that characterize the dense phase of the ISM and that define the dust accretion time-scale through equation (12). Our approach is to constrain their values comparing the model predictions with some observed properties of the MW, such as the current SFR, the existing $M_{\rm ISM}$ and M_{*}, $M_{\rm ISM}^{\rm MC}$, Z, $M_{\rm d}$ inferred from observations targeting regions of larger column densities (that we associated with the MC phase) and regions of lower column density (that we associate to the diffuse phase). In Table 1, we list the observational data that we have collected from the literature. Fig. 4 shows the results obtained for the selected set of reference parameter values listed in Table 2. Each line plotted in the figures has been obtained averaging over 50 independent merger trees of the MW, with shaded regions (where present) showing the 1σ dispersion. In the left-hand panel of Fig. 4, we show the evolution of the total gas, stellar, metal and dust masses in the ISM of the MW, where at $z > 0$ the quantities have been obtained summing over all the individual MW progenitors present at the corresponding redshift. The set of reference parameters selected leads to a final MW stellar and gas masses of $M_{*} = 7 \times 10^{10}\,M_{\odot}$ and $M_{\rm ISM} = 9 \times 10^{9}\,M_{\odot}$, in good agreement with the observational data (see Table 1). Similarly good is the agreement between the predicted final masses of metals, $M_{\rm Z} = 2.7 \times 10^{8}\,M_{\odot}$, and dust $M_{\rm d} = 1.1 \times 10^{8}\,M_{\odot}$, and the observational value; note that the data point representing the total mass in metals has been derived from the observed metallicity and gas mass, while the data point of the total dust mass has been computed as the sum of the observed dust masses of dense and diffuse phases (see Table 1). The predicted redshift evolution of the gas, metal and dust masses in the two phases of the ISM is shown in the middle panel of Fig. 4. It is clear that the selected values for the f and $\alpha_{\rm MC}$ parameters lead to final masses of cold dense gas and dust masses in the two phase in very good agreement with the observations. Note that the metal mass shown in this figure represents the total mass in heavy elements, summing metals in the gas phase and in dust grains. Hence, we find that in the cold dense phase dust accretion is maximally efficient,

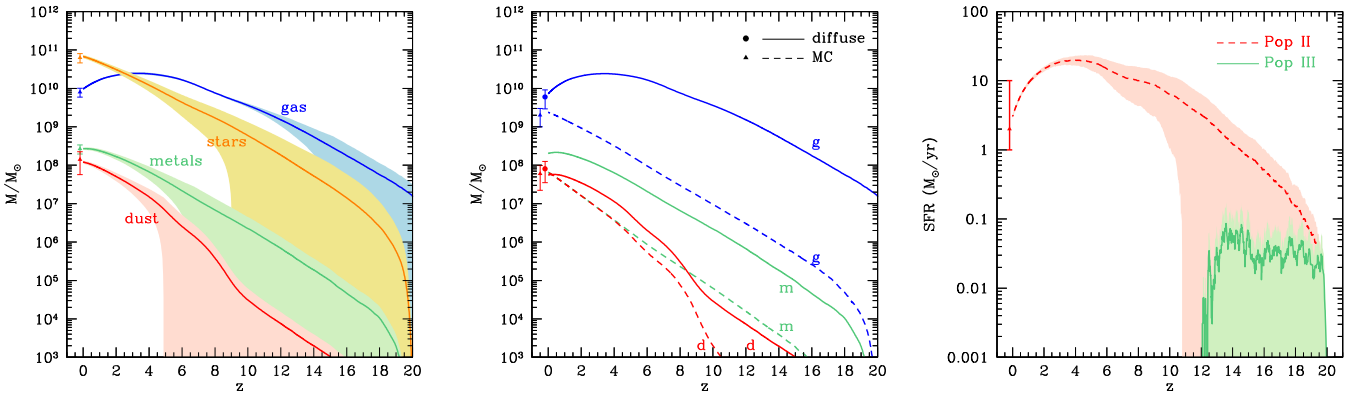

Figure 4. Redshift evolution of the predicted global properties of the MW. Each line represents an average over 50 merger-tree realizations with shaded areas representing 1σ Poissonian errors. Left-hand panel: gas (blue), star (yellow), metal (green) and dust (red) masses are shown for the fiducial model parameters of Table 2. Middle panel: separate evolution of gas (g), metals (m) and dust (d) in the diffuse (solid lines) and MC (dashed lines) ISM phase. Observed quantities at $z = 0$ are also shown (points with error bars, see Table 1). Right-hand panel: redshift evolution of Pop II (dashed red) and Pop III (solid green) SFR for model (f) (see the text and Table 3).

Table 1. Observational properties of the MW that we have used to calibrate the free parameters of the model. The existing total mass in metals and dust is derived using values in this table. Values are taken from: (a) Stahler & Palla (2004); (b) Dehnen & Binney (1998), Brown, Velásquez & Aguilar (2005); (c, d) Planck Collaboration XXV (2011); (e) Salvadori et al. (2007); (f) Ganguly et al. (2005); (g) Jenkins (2009); and (h) Chomiuk & Povich (2011).

$M_{\rm ISM}{}^a$	$M_*{}^b$	$M_{\rm d}^{\rm diff,\,c}$	$M_{\rm d}^{MC,\,d}$	$Z_{\rm ISM}{}^e$	$Z_{\rm GM}{}^f$	$Dt\,M_{\rm diff}{}^g$	SFR^h
$(8.0 \pm 2.1) \times 10^9\,{\rm M}_\odot$	$(6.3 \pm 1.7) \times 10^{10}\,{\rm M}_\odot$	$(8.07 \pm 4.56) \times 10^7\,{\rm M}_\odot$	$(6.00 \pm 3.78) \times 10^7\,{\rm M}_\odot$	${\rm Z}_\odot$	$0.25\,{\rm Z}_\odot$	0.57 ± 0.57	1–10 ${\rm M}_\odot\,{\rm yr}^{-1}$

Table 2. Model parameters adopted in the present study. The first four entries represent common parameters that have been fixed so as to match the observed global properties of the MW. The last three entries show the adopted values for the critical parameters that control the Pop III/II transition.

ϵ_*	$\epsilon_{\rm w}$	$\alpha_{\rm MC}$	f	$Z_{\rm cr}$	$\mathcal{D}_{\rm cr}$	$D_{\rm trans,\,cr}$
0.8	0.0016	1.02	0.4	$10^{-3.8}\,{\rm Z}_\odot$	4.4×10^{-9}	-3.5

i.e. at the final redshift all the metals in the gas phase are depleted on dust (the green-dashed and red-dashed curves overlap). In the right-hand panel of Fig. 4, we also show the predicted redshift evolution of the SFR, separating the contribution of Pop III and Pop II stars to the total SFR. As already described in Section 2.1, we assume that only gas in the diffuse phase can be completely ejected out of the halo, as a consequence of mechanical feedback from SNe. Hence, while the gas in the dense molecular phase can be heated and dispersed in the diffuse phase, it is not ejected out of the halo. We explored different mass-loading prescriptions of SN-driven outflows (e.g. assuming that the ejected gas is composed by different mass fractions of diffuse and dense gas), and we find that the results of the model are very similar once a re-calibration of the parameter $\alpha_{\rm MC}$ is made so as to reproduce the existing molecular mass in the MW (see Table 1).

4 PROPERTIES OF THE MILKY WAY PROGENITORS

Once the free parameters of the model are constrained, we can analyse the properties of the MW progenitors. The idea is to test if the relations between the dust/metal/gas masses that we predict for our reference model at different evolutionary stages are consistent with the observed scaling relations. Most of the available data refer to galaxies of different masses in the Local Universe. Hence, a meaningful comparison between MW progenitors at different redshifts and present-day galaxies requires that sources with comparable stellar/dust/gas masses are identified. Hence, we apply different mass selection criteria to the MW progenitors depending on the specific data sample that we consider, as it will be discussed below.

The first sample that we compare with has been recently analysed by Corbelli et al. (2012). It refers to galaxies in the Virgo cluster that have been mapped by the *Herschel* satellite (HeViCS; Davies et al. 2010), observed at 21 cm and in the CO (1–0) line. The sample comprises 35 late-type galaxies in a dynamical range $\log\,(M_{\rm gas}/{\rm M}_\odot) = 8$–$10$. Selecting MW progenitors in the same dynamical range at all redshifts, in the left-hand and middle panels of Fig. 5 we compare the model predictions with observations. The behaviour of the simulated progenitors is globally consistent with observed data, with a slope close to the proposed linear regression (dashed lines). The correlation between the dust mass and total gas mass shows that MW progenitors are generally more gas rich than typical galaxies in the observed sample, probably as a consequence of the earlier evolutionary stages of the model galaxies, which lie in the redshift range $0 < z < 4$. It is important to note that galaxies in the Corbelli et al. (2012) sample have been classified to be H I deficient, probably due to galaxy interactions in the cluster environment where they are embedded. Indeed, the model galaxies show a correlation between the dust and molecular gas masses very close to the observations, while, for a given dust mass, the predicted H I masses are generally a factor of $\sim$2 larger than observed. This is further confirmed by looking at the middle panel of Fig. 5 where we represent – for the same sample galaxies – the correlation between the dust-to-gas mass ratio and the stellar mass. Model predictions

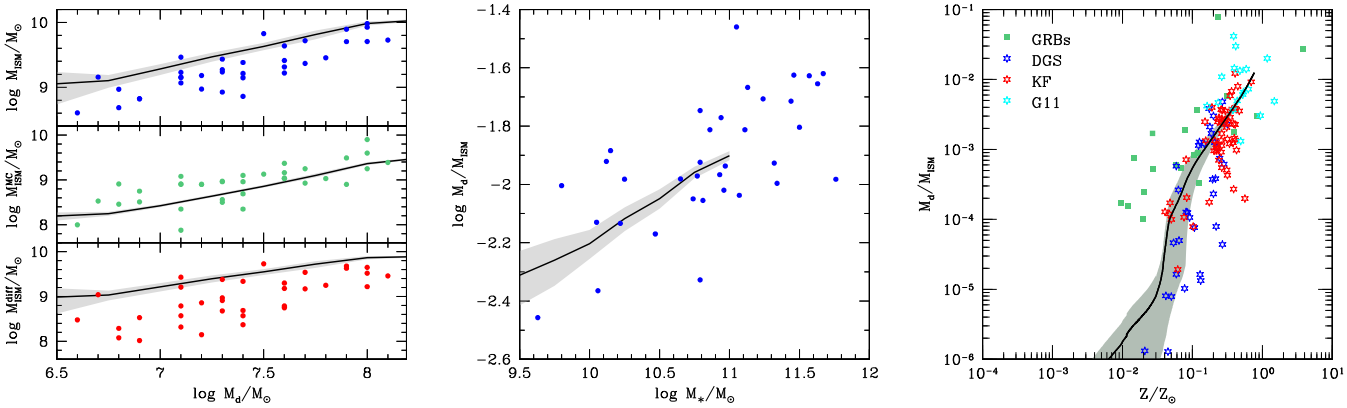

Figure 5. Comparison between the predicted properties of MW progenitors and observations. The solid lines represent averages over 50 independent merger histories of the MW and shaded region the 1σ dispersion. In the left-hand and middle panels the observational data are taken from Corbelli et al. (2012) with dashed lines indicating the best-fitting linear relation for the data. In the right-hand panel, stars refer to the sample analysed by Rémy-Ruyer et al. (2014) and squares indicate the GRB data sample of Zafar & Watson (2013, see the text). Left-hand panel: correlation between the dust mass and the diffuse, molecular and total gas masses (from bottom to top). Middle panel: dust-to-gas mass ratio as a function of the stellar mass. Right-hand panel: dust-to-gas mass ratio as a function of the gas metallicity.

show that MW progenitors are characterized by a dust-to-gas ratio that grows with the stellar mass, consistent with the observations. Yet, predicted stellar masses are smaller than $M_* \leq 7 \times 10^{10}\,\mathrm{M}_\odot$, which is the final stellar mass predicted for the MW at $z = 0$. Hence, we conclude that although the Corbelli et al. (2012) sample comprises late-type galaxies in the Virgo clusters, 30 per cent of which have stellar masses larger than the MW progenitors investigated by the present model, the general scaling relations that have been inferred from the observations are well reproduced, with differences that can be ascribed to environmental or evolutionary effects.

Additional constraints on the model can be obtained by comparing the predicted correlation between the dust-to-gas ratio and the gas metallicity. Recently, this correlation has been measured over a large metallicity range using different samples of local galaxies, such as the KINGFISH survey (Kennicutt et al. 2011), the sample collected by Galametz et al. (2011, hereafter G11), and the Dwarf Galaxy Sample (Madden et al. 2013). In the right-hand panel of Fig. 5, we show the data points from these three surveys as recently collected by Rémy-Ruyer et al. (2014). For a comparison, we also show in the same plot the data collected by Zafar & Watson (2013) over a wide redshift range $0.1 < z < 6.3$ using gamma-ray burst (GRB) afterglows. Note that while the dust masses in local samples have been inferred from the far-infrared/sub-mm emission, GRB afterglows allow us to investigate the evolution of dust content in their host galaxies using extinction data. In particular, following Kuo, Hirashita & Zafar (2013), for each GRB we consider the best-fitting extinction curve (Large Magellanic Cloud, Small Magellanic Cloud or MW like) and compute the dust-to-gas ratio from the observed optical depth and gas column density, using the corresponding correction factor. The observed data points indicate that the dust-to-gas ratio grows with the metallicity but with a large scatter, particularly at the lowest metallicities. A similar behaviour is found for the simulated MW progenitors. At low metallicities, dust and metal enrichment proceed proportionally to the stellar yields. When $Z \sim 0.02\,\mathrm{Z}_\odot$, the accretion time-scale is $\tau_{\rm acc} < 100\,\mathrm{Myr}$, gas-phase metals accretion on dust grains becomes efficient, steepening the correlation between the dust-to-gas ratio and the metallicity, which is mostly driven by grain growth in dense MCs (Asano et al. 2013; Kuo et al. 2013; Zhukovska 2014). Once all gas-phase metals are accreted, a saturation condition is reached and the simulated behaviour is driven again by the corresponding stellar yields.

5 STELLAR ARCHAEOLOGY

Hence, we have identified nine different models that we have tested against the observations: these models are characterized by a common set of parameters (calibrated to match the observed properties of the MW, as discussed in Section 3) but differ by the adopted Pop III stellar mass range and/or Pop III SN yields, and by the assumed criterion controlling the Pop III/II transition. In Table 3, we list the properties of each model, identified by a letter running from (a) to (i).

5.1 Constraints on the Pop III IMF

In Fig. 6, we show a comparison between the observed low-metallicity tail of the MDF and the theoretical prediction obtained by each of the nine models. Note that we take into account the mass- and metallicity-dependent stellar lifetimes to predict the number of stars that survives down to $z = 0$. Since at $[\mathrm{Fe/H}] \geq -2$ disc stars can contaminate the sample, the simulated MDF is truncated above $[\mathrm{Fe/H}] = -2$ and it is normalized to the total number of stars observed at $[\mathrm{Fe/H}] \leq -2$. The data points refer to the joint HK/HES sample (Beers & Christlieb, private communication) that has already been used in previous theoretical works (Salvadori et al. 2007; 2009). For completeness, we have added to the above sample the five hyper-iron-poor stars currently known: HE 0557−4840 ($[\mathrm{Fe/H}] = -4.75$; Norris et al. 2007), SDSS J102915+1172927 ($[\mathrm{Fe/H}] = -4.99$; Caffau et al. 2011b, 2012), HE 1327−2326 ($[\mathrm{Fe/H}] = -5.76$; Frebel et al. 2005), HE 0107−5240 ($[\mathrm{Fe/H}] = -5.54$; Christlieb et al. 2004), and the recently discovered SMSS J031300 ($[\mathrm{Fe/H}] < -7.1$; Keller et al. 2014).

Let us focus on the first row of Fig. 6, which shows models where the Pop III/II transition is driven by a critical metallicity of $Z_{\rm cr} = 10^{-3.8}\,\mathrm{Z}_\odot$ (Salvadori et al. 2007), differing only for the adopted Pop III IMF and corresponding yields (see Table 3). In model (a) we assume that Pop III stars form in the mass range [10–300] $\mathrm{M}_\odot$ according to a Larson IMF with $m_{\rm ch} = 20\,\mathrm{M}_\odot$. Hence, in this model the two mass ranges where Pop III stars contribute to metal and dust enrichment are $10\,\mathrm{M}_\odot \leq m_* \leq 40\,\mathrm{M}_\odot$, where we adopt yields of ordinary cc SNe, and $140\,\mathrm{M}_\odot \leq m_* \leq 260\,\mathrm{M}_\odot$, where the stars explode as PISNe. The resulting MDF is very similar to what was found by previous investigations (see fig. 6 in Salvadori et al. 2007), where a 200 $\mathrm{M}_\odot$ single-mass Pop III IMF was adopted. This is not surprising because even if we have enlarged the Pop III stellar mass range and relaxed the Instantaneous Recycling Approximation (IRA), the IMF-weighted yields are very similar to those of a single 200 $\mathrm{M}_\odot$ PISN. For this model, the bulk of observed stars at $[\mathrm{Fe/H}] \gtrsim -4$ is very well reproduced, but no star is predicted with $[\mathrm{Fe/H}] < -4$, at odds with the observations. Note that four out of the five stars currently known with $[\mathrm{Fe/H}] < -4.5$ are CEMP, hence for these stars [Fe/H] is not a good metallicity indicator. Although the interpretation of the origin of CEMP stars is complicated by the fact that these stars do not represent a homogeneous class (see the discussion in Section 5.3), Pop III SNe in which mixing was minimal and fallback was large have been shown to provide a good match to the observed abundance pattern (Umeda & Nomoto 2002; Tominaga, Umeda & Nomoto 2007; Joggerst, Woosley & Heger 2009; Kobayashi, Tominaga & Nomoto 2011; Keller et al. 2014). In these so-called faint SNe, the small iron abundance reflects the fact that iron failed to be mixed sufficiently far out to be ejected.

Hence, in model (b) we have adopted the same Pop III IMF as in model (a), but assuming that Pop III stars with masses in the range $10\,\mathrm{M}_\odot \leq m_* \leq 40\,\mathrm{M}_\odot$ explode as faint cc SNe and contribute to metal and dust enrichment with their specific carbon-rich and iron-poor yields, that we take from the recent study by Marassi et al. (2014). The resulting MDF is shown in the second

Table 3. In this table, we identify the models that we have investigated varying the Pop III stellar IMF, the adopted SN yields and the Pop III/II transition criterion.

Model name	(a)	(b)	(c)	(d)	(e)	(f)	(g)	(h)	(i)
Pop III IMF	PISN+cc	PISN+faint	faint	PISN+cc	PISN+faint	faint	PISN+cc	PISN+faint	faint
Pop III/II transition	$Z_{\rm cr}$	$Z_{\rm cr}$	$Z_{\rm cr}$	$\mathcal{D}_{\rm cr}$	$\mathcal{D}_{\rm cr}$	$\mathcal{D}_{\rm cr}$	$D_{\rm trans,\,cr}$	$D_{\rm trans,\,cr}$	$D_{\rm trans,\,cr}$

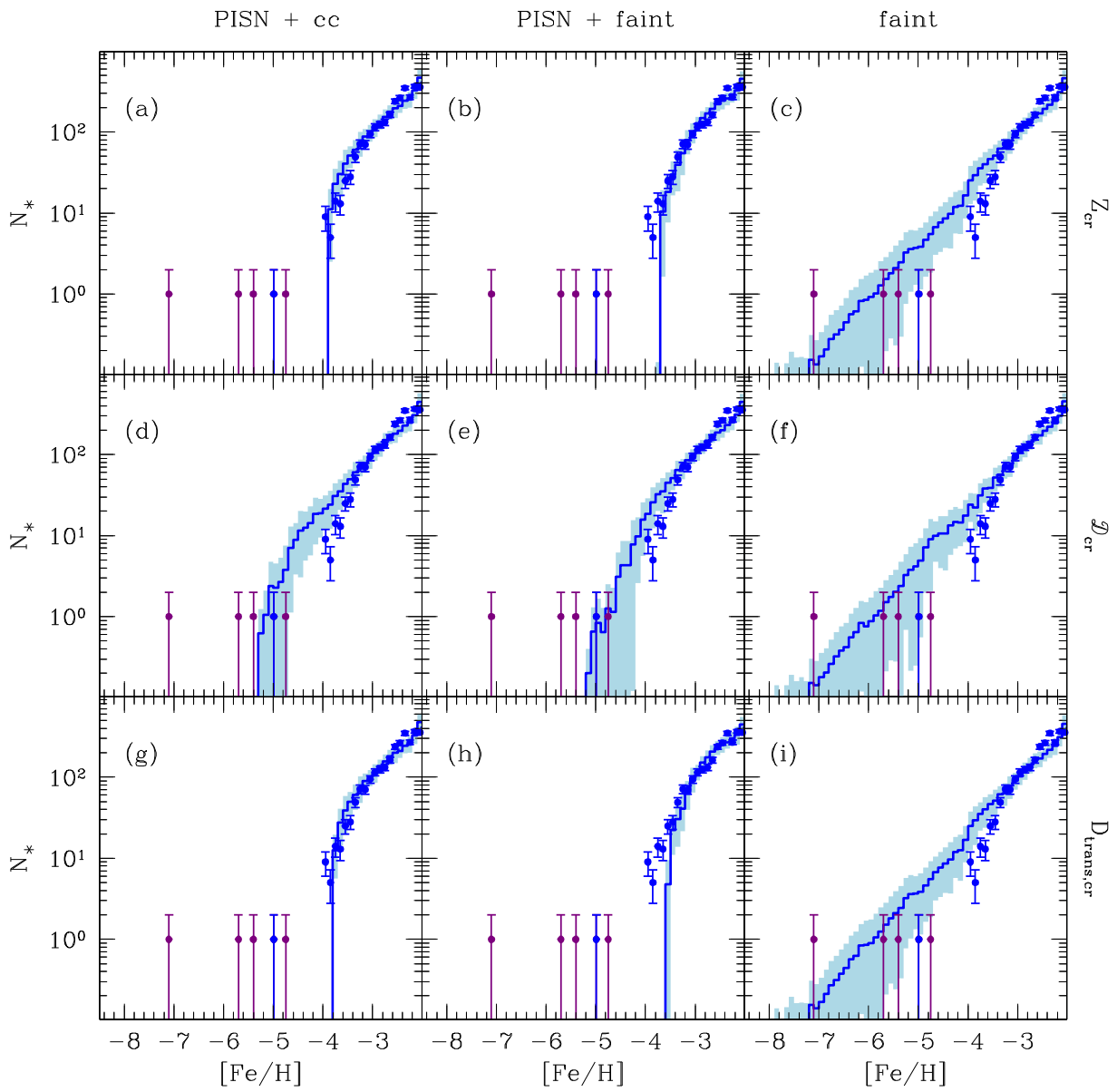

Figure 6. Simulated MDF averaged over 50 merger trees (solid line) with 1σ dispersion (shaded area) for different Pop III IMF (columns) and for different transition criteria (rows). Points are the observed MDF as in Salvadori et al. (2007) with Poissonian error bars, distinguishing between C-normal (blue) and CEMP (purple) stars. The Pop III/II transition is parametrized with: a critical metallicity (first row) $Z_{\rm cr} = 10^{-3.8}\,{\rm Z}_{\odot}$ (Salvadori & Ferrara 2012); a critical dust-to-gas ratio (second row) $\mathcal{D}_{\rm cr} = 4.4 \times 10^{-9}$ (Schneider et al. 2012a); a critical transition discriminant (third row) $D_{\rm trans,\,cr} = -3.5$ (Frebel & Norris 2013). The Pop III IMF is taken to extend to: 300 $\rm M_{\odot}$ with cc SNe (first column); 300 $\rm M_{\odot}$ with faint SNe (second column); 140 $\rm M_{\odot}$ with faint SNe (third column). Note that three hyper-iron-poor stars are added with respect to the observed MDF in Salvadori et al. (2007): HE 0557−4840 ([Fe/H] ≈ −4.75; Norris et al. 2007); SDSS J102915+172927 ([Fe/H] ≈ −4.99; Caffau et al. 2011b, the only C-normal star among the hyper-iron-poor stars); SMSS J031300 ([Fe/H] $\lesssim$ −7.1; Keller et al. 2014).

top panel of Fig. 6 and appears to be almost identical to that of model (a); in fact, PISN largely dominate the Fe production and – being more massive – are the first Pop III stars to enrich the ISM. By the time the first faint SNe explode, the gas is already enriched in Fe and their contribution to the low-[Fe/H] tail of the MDF becomes negligible. Hence, the lowest [Fe/H] bin populated by stars in the theoretical MDF is related to the PISN iron yield, and the observed stars at [Fe/H] < −4.5 are still not reproduced by the model.

If we limit the mass range of Pop III stars to [10–140] $\rm M_{\odot}$, excluding the PISN progenitors mass range, we find the results shown in the third top panel (model c). Iron enrichment is much slower than previous cases, being dominated by faint SNe. As a result, the tail of the MDF extends down to [Fe/H] ∼ −8, well into the observed range of the most iron-poor stars. Although for this model the average MDF agrees with the observations at [Fe/H] ≤ −4.75 and at [Fe/H] ≥ −3.5, at least within the 1σ scatter, there is a clear excess of stars with −4.75 < [Fe/H] < −3.5 with respect to the data, which indicate a sharp change of slope in the MDF. The smooth, continuous growth of the simulated MDF for −8 ≤ [Fe/H] ≤ −2 suggests that additional physical processes, beyond those implemented in the present study, are at work. Most notably, radiative

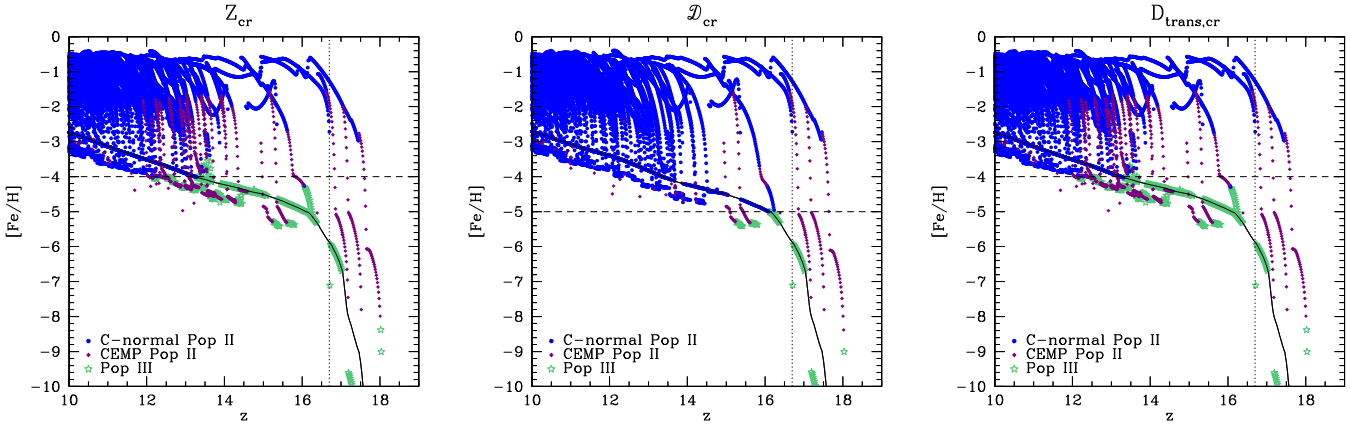

Figure 7. Redshift evolution of the [Fe/H] within MW progenitors for a single merger-tree realization for models (c), (f), and (i) (from left to right). Green stars identify MW progenitor haloes that are forming Pop III stars, while filled purple diamonds and filled blue dots are progenitor haloes forming carbon-enhanced and carbon-normal Pop II stars, respectively. The black solid line represents the evolution of the [Fe/H] of the GM. The vertical dotted lines indicate the redshift at which the GM is characterized by [C/Fe] > 1.0, so that the gas in haloes virializing from the GM after this redshift are characterized by a C-normal elemental abundance. The horizontal dashed lines represent the [Fe/H] at which the GM exceeds the value of the critical parameter controlling the Pop III/II transition.

feedback effects that may prevent the gas in the first minihaloes from cooling, delaying or inhibiting star formation (Karlsson 2006; Salvadori & Ferrara 2012; de Bennassuti et al. in preparation).

5.2 Constraints on the Pop III/II transition

The second and third rows of Fig. 6 show – for the same set of Pop III IMF and SN yields discussed above, the predicted MDF when the Pop III/II transition occurs above a minimum dust-to-gas ratio or transition discriminant. Models (d) and (e) show that the condition $\mathcal{D} \geq \mathcal{D}_{\rm crit}$ allows to populate the MDF down to [Fe/H] ~ -5.4 even when Pop III stars are assumed to form with masses [10–300] $M_\odot$ and independently of the adopted cc SN yields. Yet, even in this case the mass range of PISN progenitors has to be excluded from the Pop III IMF in order to reproduce the low-[Fe/H] tail down to the lowest observed values (model f).

Finally, for a given Pop III IMF and SN yields, a Pop III/II transition occurring when $D_{\rm trans} > D_{\rm trans,\,crit}$ does not lead to appreciable differences in the MDF with respect to models where low-mass stars form when $Z > Z_{\rm cr}$ (compare models g, h, i, with models a, b, c, respectively). In conclusion, faint SNe are needed to reproduce the low-metallicity tail of the MDF.

In Fig. 7, we show the redshift evolution of the [Fe/H] within MW progenitor haloes selected from a single merger-tree realization, whose results at $z = 0$ are most similar to the average ones. The three panels refer to models which adopt the same Pop III IMF([10–140] $M_\odot$ mass range with faint SNe) but different Pop III/II transition criteria (models c, f, and i, from left to right). Depending on the gas properties, at each time, individual MW progenitors can either form Pop III stars (green starred points) or Pop II stars (C normal or C enhanced). Following the definition of Beers & Christlieb (2005), metal-poor stars are classified as CEMP if [C/Fe] ≥ 1. The solid black line represents the [Fe/H] evolution in the GM. Points along this line identify haloes that have virialized from the GM and that form stars for the first time; hence their gas properties reflect the corresponding properties of the GM at that redshift. At each given redshift, points above the black solid line represent haloes that have been self-enriched by their stellar populations or that have inherited their [Fe/H] through mergers with highly enriched progenitors. Conversely, points below the black solid line represent progenitors whose [Fe/H] has been diluted below the GM value by mergers with un-polluted haloes (that have virialized at an earlier epoch but have not formed stars yet). The horizontal-dashed and vertical-dotted lines mark two important evolutionary phases: the first one identifies the [Fe/H] when the critical Pop III/II transition criterion is met in the GM. Hence, haloes that virialize after this epoch can only form Pop II stars (see the transition from starred points to dots along the GM line). This occurs at different epochs in the three models as a consequence of the different Pop III/II transition criteria (at $z \sim 14$ for models c and i, and at $z \sim 16$ for model f). The nature of the first Pop II stars that form in newly virialized haloes depends on the [C/Fe] content of the GM: the vertical-dotted line marks the redshift at which [C/Fe] $= 1$; for all the three models, the first Pop II stars that form in newly virialized haloes are always C normal. The typical evolutionary tracks in the first progenitors show that Pop III stars continue to form until the first faint SNe explode and enrich the ISM above the critical threshold for Pop II star formation. The first Pop II stars are typically C enhanced, reflecting the yields of faint SNe. Once the first Pop II cc-SNe explode, the [C/Fe] is decreased to <1 and the subsequent generations of Pop II stars are C normal.

Comparing the three panels, it is evident that when [Fe/H] < -5 the evolutionary tracks do not depend on the transition criterion, resulting in a very similar low-[Fe/H] tail of the MDF. The major difference is in the duration of the Pop III star formation epoch, that is shorter when a dust-driven transition is adopted. As a result, in model (f) C-normal Pop II stars can form at $-5 <$ [Fe/H] < -4 due to early enrichment from Pop II cc SNe. Conversely, in models (c) and (i) a larger fraction of Pop II stars are C enhanced due to the larger contribution to gas enrichment from faint Pop III SNe. Hence, tighter constraints on the Pop III/II transition can be set by separating the contribution to the MDF of C-normal and C-enhanced stars. The results are shown in Fig. 8. It is clear that CEMP stars dominate the low-[Fe/H] tail of the simulated MDF for all three models, as a result of the dominant role played by Pop III faint-SN in the first metal enrichment. However, it is only in model (f), where Pop II stars form when $\mathcal{D} \geq \mathcal{D}_{\rm crit}$, that the MDF of C-normal stars extends to [Fe/H] ~ -5.4, accounting for the observed data point that corresponds to SDSS J102915+172927, the only C-normal star at these low [Fe/H] currently known (Caffau et al. 2011b). Note that the predicted [C/Fe] for C-normal stars with [Fe/H] < -4.5 ranges between 0 and +1, consistent with the observed properties

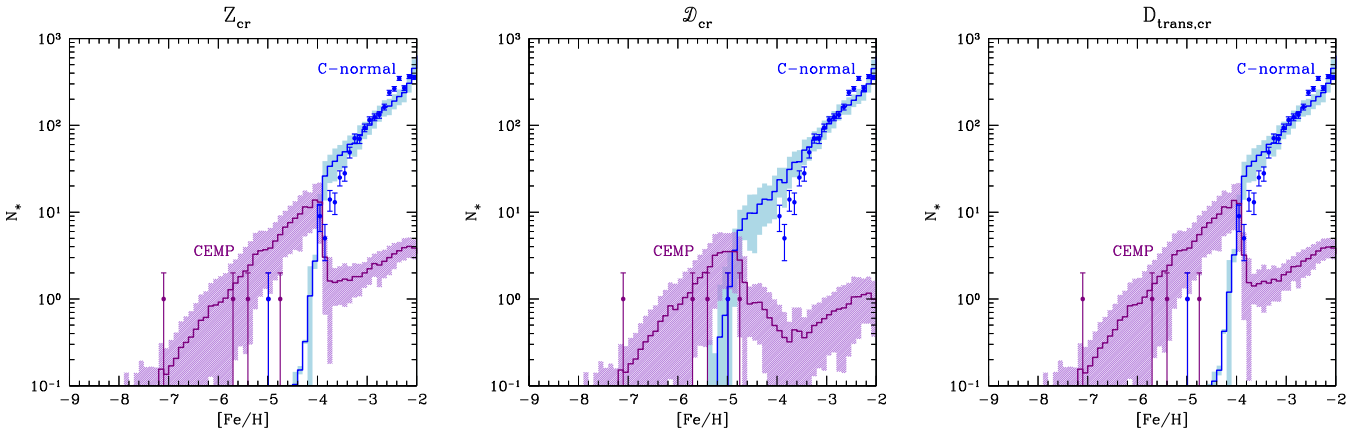

Figure 8. The contribution of C-enhanced stars ([C/Fe] $\geq$ 1.0, purple line and shaded region) and C-normal stars ([C/Fe] $<$ 1, blue line and shaded region) to the theoretical MDF for models (c), (f) and (i) (from left to right, see the text).

of SDSS J102915+172927 (Caffau et al. 2011b). Conversely, the MDF of C-normal stars predicted by models (c) and (i) do not extend below [Fe/H] ~ -4.5. Hence, as already discussed by Caffau et al. (2011b), Schneider et al. (2012b) and Klessen, Glover & Clark (2012), the formation of SDSS J102915+172927 must have followed alternative pathways, beyond that associated with fine-structure line cooling.

We conclude that the observed MDF at [Fe/H] ≤ -2 and the relative fraction of C-normal and C-rich stars at [Fe/H] ≤ -4.5 seem to indicate model (f) as the best-fitting scenario, where the transition is driven by the dust-to-gas ratio, Pop III stars preferentially form in the mass range [10–140] $M_{\odot}$ and explode as faint SNe. The contribution of PISN to the first enrichment, if present, must have been largely subdominant. Finally, the formation of the first low-mass stars must have been triggered by processes occurring at metallicities below those normally assumed to enable efficient fine-structure line cooling, such as by dust cooling and fragmentation. Other models can be excluded because they do not predict the existence of stars and/or C-normal stars below [Fe/H] < -4, at odds with observations.

5.3 Carbon enhancement

Spectroscopic studies of metal-poor stars in the HK, HES and more recently SDSS samples have convincingly shown that the frequency of CEMP stars grows with decreasing [Fe/H], being $\sim$20 per cent at [Fe/H] < -2 and as large as 80 per cent at [Fe/H] < -4 (Lee et al. 2013; Norris et al. 2013; Spite et al. 2013; Yong et al. 2013b). However, the increasing frequency of CEMP stars with declining [Fe/H] is not equally important for the different subclasses which characterize CEMP stars. Generally, CEMP stars are classified as CEMP-s/rs and CEMP-no (Beers & Christlieb 2005) depending on the overabundant presence of s or rs-process elements (such as Ba, Sr, Eu) or no overabundance of neutron-capture elements. It has been suggested that these differences may provide clues to the nature of their likely progenitors. In particular, CEMP-s and CEMP-rs have abundance patterns that suggest mass transfer from an AGB companion in a binary system (Suda et al. 2004; Masseron et al. 2010). Indeed, long-term radial-velocity observations show that a large percentage of CEMP-s/rs stars are binaries (Lucatello et al. 2005). However, the abundance pattern of the CEMP-no stars is difficult to explain as caused by a mass transfer from an AGB companion and the nature of their progenitors is still largely debated. Using a homogeneous chemical analysis of 190 metal-poor stars Yong et al. (2013a) and Norris et al. (2013) have recently investigated a sample of CEMP-no stars with [Fe/H] < -3. They conclude that the observed chemical abundances are best explained by models which invoke the nucleosynthesis of Pop III SNe with mixing and fallback, the so-called faint SNe that we have discussed in Section 5.1. In addition, observations show that the relative fraction of CEMP-no and CEMP-r/rs stars depends on [Fe/H], with CEMP-no stars representing the large majority ($\sim$90 per cent) of CEMP stars at [Fe/H] < -3 (Aoki et al. 2007; Masseron et al. 2010).

In the left-hand panel of Fig. 9, we show [C/H] as a function of [Fe/H] for 86 stars with [Fe/H] < -3 out of the full sample of 190 stars analysed by Yong et al. (2013a, see their table 1), to which we have added SDSS J102915+1172927 (Caffau et al. 2011b) and SMSS J031300 (Keller et al. 2014), that were not present in the original sample. Following Norris et al. (2013), we have divided the sample into CEMP-no and CEMP-r/s stars, where the latter class includes CEMP-s, CEMP-r, and CEMP-rs stars. The grey shaded area marks the region of the plane where the stars are classified as C normal ([C/Fe] < 1, according to our definition). It is clear from the figure that CEMP-no stars represent the dominant population of CEMP stars at [Fe/H] < -4.5, but that the number of CEMP-r/s stars grows with [Fe/H] and become the dominant class of CEMP stars at [Fe/H] > -3.5. This is clearly seen in the right-hand panel of the same figure, where we plot the observed fraction of CEMP stars (number of CEMP stars divided by the total number of stars) and of CEMP-no stars for four different [Fe/H] bins. To be consistent with Yong et al. (2013b), we have considered a single bin for the five hyper-iron-poor stars with [Fe/H] < -4.5 and then three bins in the $-4.5 \leq$ [Fe/H] ≤ -3 range, chosen to contain an almost equal number of stars ($\sim$28, 27, and 28 from the lowest to the highest [Fe/H] bin). Open data points refer to the fraction of CEMP stars and filled data points to the fraction of CEMP-no stars only. We find that the fraction of CEMP stars decreases from 0.8 to 0.3, but that the decrease becomes much steeper when only CEMP-no stars are considered, going from $\sim$80 per cent to less than 5 per cent. Yet, the predicted fraction of CEMP stars for the fiducial case (f) shows an even steeper decline. It is important to stress that in our model CEMP stars can form only as a result of the enrichment from Pop III faint SNe, as we do not consider mass-transfer effects in stellar binaries. Hence, strictly speaking, we cannot predict the existence of CEMP-r/s stars and the simulated data must be compared only to the CEMP-no fraction. However, while the model is

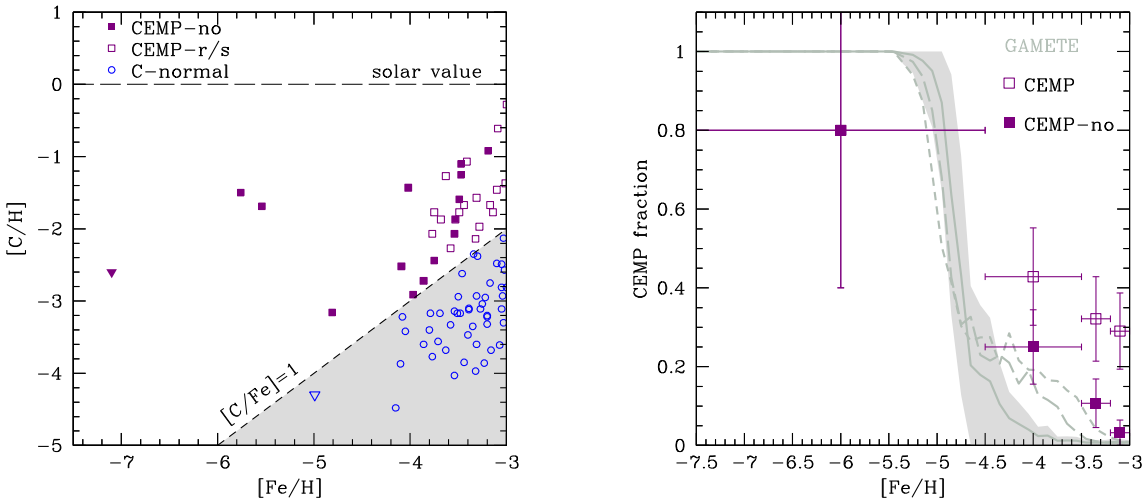

Figure 9. Left-hand panel: C abundance as a function of [Fe/H] for the C-normal (open blue points), CEMP-no (filled purple squares) and CEMP-r/s (open purple squares) stars taken from the sample of Yong et al. (2013a). We also added to their sample the CEMP-no SMSS J031300 star (purple filled triangle; Keller et al. 2014) and the C-normal SDSS J102915+1172927 star (blue open triangle; Caffau et al. 2011b, 2012). The dashed line corresponding to [C/Fe] = 1 marks the separation between C-normal (grey area) and C-rich stars, following the definition of Beers & Christlieb (2005). The horizontal dashed line shows the solar C abundance. Right-hand panel: observed fraction of CEMP (open squares) and CEMP-no (filled squares) stars in four different [Fe/H] bins. Error bars on the *y*-axis represent Poissonian errors on the number of stars in each bin and on the *x*-axis reflect the amplitude of the [Fe/H] bin (see the text). The grey solid line shows the predicted fraction of CEMP-no stars for the fiducial model (f) averaged over 50 merger trees. The shaded region shows the 1σ dispersion among different merger histories. The long-dashed and dashed lines show the results obtained when 30 and 50 per cent of the Type II SN progenitors are assumed to explode as faint SNe, respectively.

consistent with the data (within 1σ) for three out of the four [Fe/H] bins, it underpredicts the fraction of CEMP-no stars at [Fe/H] ≥ -4.5. We will further discuss this point in the next section. Here, we comment on the fact that we have conservatively assumed that only Pop III stars can end their life as faint SNe, whereas faint SNe have been directly observed in the local Universe, like SN 1997D (Turatto et al. 1998), which has been considered as a prototype for this class of objects, and many more examples (see the compilation in Pastorello et al. 2006; Fraser et al. 2011), including the dimmest sources SN 1999br (Pastorello et al. 2004) and SN 2010id (Gal-Yam et al. 2011). Additional indication that a population of faint SNe may exist come from the non-detection of SNe associated with low-redshift long GRBs (Della Valle et al. 2006). It is difficult to directly estimate the fraction of faint SN from current SN data, due to the bias against dim sources in present samples. Using very local ($\leq$10 Mpc) data, Horiuchi et al. (2011) have estimated that the fraction of dim SNe, defined as SNe with an absolute magnitude of $M > -15$, ranges between 3 and 20 per cent. However, they also find that a fraction as large as 30–50 per cent is required in order to reconcile the observed SN rate with that predicted from the observed cosmic SFR. Assuming a similar fraction of Pop II faint SNe we can better match the observed data points, as shown in Fig. 9.

6 DISCUSSION

Several theoretical models aimed to investigate the early enrichment and star formation history of the MW have been developed and compared to observations of the most metal-poor stars in the Galactic halo and nearby dwarf galaxies.

Tumlinson (2006) and Salvadori et al. (2007) first applied semi-analytic approaches to hierarchical structure formation to follow the chemical enrichment of the MW and to put constraints on the properties of the first stars. Tumlinson (2006) explored different Pop III IMFs and found good agreement with the Galactic halo MDF for top-heavy IMFs sharply peaked in the mass range of cc SNe, [12–70] $M_\odot$, and for $Z_{cr} \sim 10^{-4}\,Z_\odot$. Salvadori et al. (2007) investigated the Pop III/II transition by adopting different Z_{cr} values and Pop III masses. They showed that the persistent non-detection of metal-free stars implies that Pop III stars have masses $m > 0.9\,M_\odot$, or that $Z_{cr} > 0$. By assuming that Pop III stars explode as PISN, moreover, they found that a value of $Z_{cr} \sim 10^{-4}\,Z_\odot$ is required to correctly reproduce the observed MDF at [Fe/H]>-4, although the existence of hyper-iron-poor stars cannot be explained. By using an upgraded version of the model, which includes the physics of minihaloes along with an analytical prescription to account for the inhomogeneous reionization and metal enrichment of the GM, Salvadori & Ferrara (2012) showed that the low-Fe tail of the Galactic halo MDF shifts towards lower [Fe/H] values when Pop III stars are assumed to explode as faint SNe of $m = 25\,M_\odot$ (Kobayashi et al. 2011). By studying the chemical abundances of very metal-poor damped Lyα absorption systems in the context of the MW formation, these authors demonstrate that faint SNe dominate the chemical enrichment at [Fe/H]<-5, while at higher [Fe/H] the gas (and stars) chemical abundances are only partially imprinted by this pristine stellar generation.

Tumlinson (2007) considered an IMF dependent on the temperature of the CMB as a way to explain the [Fe/H] dependence of CEMP-s/rs stars, assumed to form in stellar binaries. Komiya 2011; Komiya et al. (2009, 2010) addressed the difference between the hyper-iron-poor stars at [Fe/H] < -4.5 and stars with [Fe/H] > -4.5 in the context of hierarchical galaxy formation: they examine the possibility that hyper-iron-poor stars could originate by low-mass Pop III stars whose surface is polluted by accretion of enriched gas from the halo ISM. They discussed the total number of stars with [Fe/H] < -3 as well as the shape of the MDF and found the best agreement for a high-mass IMF (assumed to be the same for all stellar populations) and accounting for the formation of stellar binaries, without evoking a transition in the stellar IMF. Additionally,

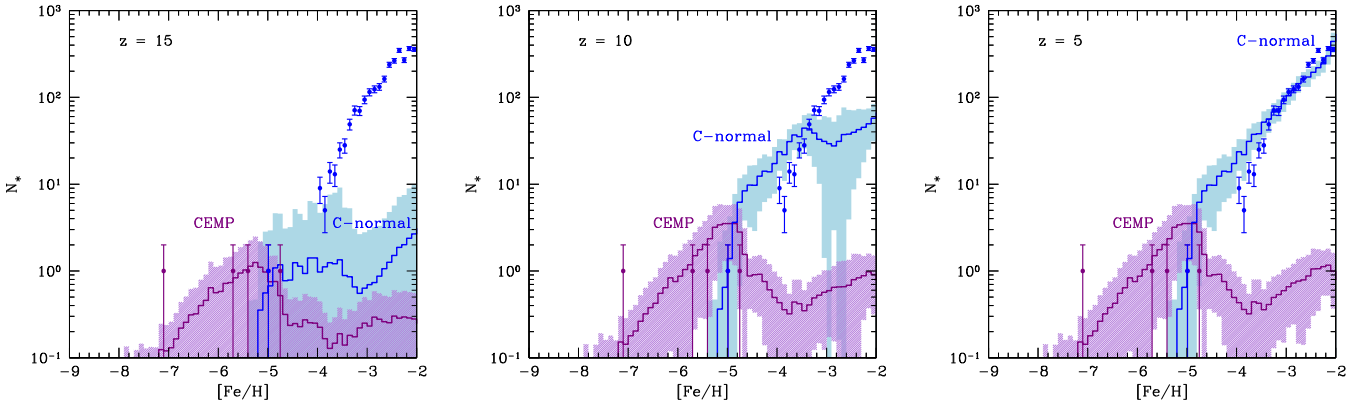

Figure 10. Redshift evolution of the MDF for the fiducial model (f), separating the contribution of CEMP and C-normal stars ($z = 15$, 10, 5 from left to right).

they explored different SN yields obtaining good fit to the MDF for all adopted SNe nucleosynthesis model.

Very recently, Cooke & Madau (2014) have suggested that carbon-enhanced metal-poor stars may originate in minihaloes polluted by low-energy SNe which produce a supersolar ratio of [C/Fe]. Conversely high-energy SNe that produce a near-solar ratio of [C/Fe] completely unbound the gas in the first minihaloes, thereby suppressing the formation of a second generation of stars. The recent detection of SDSS J001820.5−093939.2, a truly second-generation star at [Fe/H] ~ -2.5 exhibiting the clear imprint of PISNe (Aoki et al. 2014), suggests that this is not the case. This observation demonstrates that these stars do exist but they are extremely rare and they are likely hidden at higher [Fe/H], as already suggested by Salvadori et al. (2007).

In this paper, we investigate the hierarchical formation of the MW and its chemical enrichment in metals, Fe, C, O. For the first time, we develop and apply a chemical evolution model in a two-phase ISM, to account for grain growth in cold, dense clouds and grain destruction in the hot, diffuse medium. This allows us to investigate the Pop III/II transition under different physical conditions, including the effect of line cooling ($Z_{\rm cr}$ or $D_{\rm trans,\,cr}$), and dust grains ($\mathcal{D}_{\rm cr}$). We explore different IMFs and different SNe yields for Pop III stars. The existence of hyper-iron-poor, carbon-enhanced stars is a strong indication that faint SNe (rather than PISNe and cc SNe, which give a too strong Fe enrichment) dominate the nucleosynthetic output of Pop III stars. The assumption of Pop III faint SNe is crucial not only to extend the tail of the MDF down to [Fe/H] < -7, but also to reproduce the dependence of the CEMP fraction on [Fe/H]. In the present study, we have not considered a binary origin of CEMP stars. For this reason, we have compared our results with observed samples excluding CEMP-s/r/rs stars; yet, as shown in Fig. 9, the fraction of CEMP stars predicted in our simulated samples tends to underpredict the observed data at $-4.5 <$ [Fe/H] < -3. As we have discussed in the previous section, the observations could be reproduced if 30–50 per cent of Pop II SNe are assumed to be faint, consistent with the observational indication of local SN samples (Horiuchi et al. 2011). The inclusion of minihaloes into the model is also expected to increase the number of carbon-enhanced stars, providing a better agreement with the data (Salvadori et al. in preparation). However, we should note that the $-4.5 <$ [Fe/H] < -3 range is where the simulated MDF provides the worst agreement with the observations, showing no sign of the observed change of slope between the roughly constant tail at [Fe/H] < -4 and the steep rise at [Fe/H] > -4. On the contrary, even for the best-fitting model, the simulated MDF is characterized by a single slope in the range $-7 <$ [Fe/H] < -2, although with an increasing scatter between different merger-tree realizations at [Fe/H] < -4. This is not surprising given that we have assumed that radiative feedback has suppressed star formation in minihaloes, which are instead predicted to be the progenitors of today lived ultrafaint dwarf galaxies (Salvadori & Ferrara 2009) and to have played a major role in the early metal enrichment and reionization of the MW environment (Salvadori et al. 2014). In the present study, instead, stars form only in haloes with virial temperatures $T_{\rm vir} \geq 2 \times 10^4$ K that can cool via Lyα cooling. Hence, the shape of the MDF at low [Fe/H] mostly reflects the efficiency of star formation and metal enrichment in these more massive progenitors. Yet, Fig. 10 shows that Pop II stars that populate the bins at $-5 <$ [Fe/H] < -3 in the simulated MDF mostly form at redshifts $15 \leq z \leq 10$, where we expect radiative feedback to play a major role in self-regulating the efficiency of star formation and metal enrichment in minihaloes (Salvadori & Ferrara 2012). A proper analysis of low-metallicity star formation in minihaloes will be the subject of a forthcoming paper (de Bennassuti et al. in preparation).

7 CONCLUSIONS

In this paper, we have presented a new version of the semi-analytical code GAMETE and some first applications of this new model to stellar archaeology. For the first time, we follow the star formation history and the enrichment in metals and dust of the MW galaxy along its hierarchical evolution. Using a two-phase description of the ISM in each progenitor galaxy of the MW, we can follow the evolution of the atomic and molecular gas components and the separate evolution of metals and dust grains in these two phases. In particular, dust grains are destroyed by interstellar SN shocks in the hot diffuse phase, but are shielded against destruction and grow in mass by accreting gas-phase metals in the dense, molecular phase. We show that:

(i) the model is characterized by four free parameters (efficiencies of star formation and SN winds and two additional parameters which regulate the mass transfer between the diffuse and molecular phases) that have been calibrated so as to reproduce the observed properties of the MW at $z = 0$.

(ii) Using this fiducial set of parameters, the simulated progenitors of the MW follow the scaling relations between the gas (total, dense and diffuse) and dust, and between the dust-to-gas ratio and stellar mass inferred from observations of Virgo cluster galaxies (Corbelli et al. 2012); in addition, it also predicts a relation between the dust-to-gas ratio and metallicity that is in very good agreement

with observations of different samples of local galaxies (Rémy-Ruyer et al. 2014) and GRB-host galaxies at $0.1 \leq z \leq 6.3$ (Zafar & Watson 2013).

(iii) When applied to stellar archaeology, the simulated MDF is very sensitive to the adopted Pop III IMF and metal yields. Current observations seem to require a largely subdominant contribution from Pop III PISN to early metal enrichment, favouring Pop III stars with masses in the range [10–140] $M_\odot$ which explode as faint SNe.

(iv) The separate contribution of C-normal and CEMP stars to the MDF is sensitive to the critical conditions that are assumed to control the Pop III/II transition. This analysis confirms the expectations that C-normal stars with [Fe/H] < -4.5, such as J102915+172927 (Caffau et al. 2011b), can form only if the transition is driven by dust, when $\mathcal{D} \geq \mathcal{D}_{\rm crit} = 4.4 \times 10^{-9}$.

(v) Our fiducial model predicts a steep decline of the CEMP fraction with [Fe/H], consistent with the data, but underpredicts the fraction of CEMP stars in the range $-4.5 \leq$ [Fe/H] ≤ -3, suggesting the additional contribution from Pop II faint SNe to C enrichment.

(vi) The change of slope in the low-[Fe/H] tail of the observed MDF cannot be explained by chemical and mechanical feedback effects, and may be due to additional physical processes that regulate the efficiency of star formation in the first star-forming regions. Most likely, radiative feedback associated with the rising UV background that inhibits star formation by photodissociating molecular hydrogen and/or suppressing gas infall in the first minihaloes.

ACKNOWLEDGEMENTS

We thank the anonymous referee for her/his positive and useful comments and suggestions. The research leading to these results has received funding from the European Research Council under the European Unions Seventh Framework Programme (FP/2007-2013)/ERC Grant Agreement no. 306476. This research was supported in part by the National Science Foundation under grant no. NSF PHY11-25915. SS acknowledges support from Netherlands Organization for Scientific Research (NWO), VENI grant 639.041.233

REFERENCES

Aoki W., Beers T. C., Christlieb N., Norris J. E., Ryan S. G., Tsangarides S., 2007, ApJ, 655, 492
Aoki W., Tominaga N., Beers T. C., Honda S., Lee Y. S., 2014, Science, 345, 6199
Asano R. S., Takeuchi T. T., Hirashita H., Inoue A. K., 2013, Earth Planets Space, 65, 213
Barkana R., Loeb A., 2001, Phys. Rep., 349, 125
Beers T. C., Christlieb N., 2005, ARA&A, 43, 531
Beers T. C., Preston G. W., Shectman S. A., 1992, AJ, 103, 1987
Bianchi S., Schneider R., 2007, MNRAS, 378, 973
Binney J., Merrifield M., 1998, Galactic Astronomy. Princeton Univ. Press, Princeton, NJ
Bromm V., 2013, Rep. Prog. Phys., 76, 11
Bromm V., Loeb A., 2003, Nature, 425, 812
Bromm V., Ferrara A., Coppi P. S., Larson R. B., 2001, MNRAS, 328, 969
Brown A. G., Velásquez H. M., Aguilar M. A., 2005, MNRAS, 359, 287
Caffau E., Ludwig H.-G., Steffen M., Freytag B., Bonifacio P., 2011a, Solar Phys., 268, 255
Caffau E. et al., 2011b, Nature, 477, 67
Caffau E., Bonifacio P., François P., Spite M., Spite F., Zaggia S., Ludwig H.-G., Steffen M., 2012, A&A, 542, 51
Carollo D. et al., 2012, ApJ, 744, 195
Cayrel R. et al., 2004, A&A, 416, 1117
Chiaki G., Schneider R., Nozawa T., Omukai K., Limongi M., Yoshida N., Chieffi A., 2014, MNRAS, 439, 3121
Chomiuk L., Povich M. S., 2011, AJ, 142, 197
Christlieb N., 2003, Rev. Mod. Astron., 16, 191
Christlieb N., Gustafsson B., Korn A. J., Barklem P. S., Beers T. C., Bessell M. S., Karlsson T., Mizuno-Wiedner M., 2004, ApJ, 603, 708
Christlieb N., Schörck T., Frebel A., Beers T. C., Wisotzki L., Reimers D., 2008, A&A, 484, 721
Ciardi B., Ferrara A., 2005, Space Sci. Rev., 116, 625
Clark P. C., Glover S. C. O., Klessen R. S., 2008, ApJ, 672, 757
Cooke R., Madau P., 2014, ApJ, 791, 116
Corbelli E., Bianchi S., Cortese L., Giovanardi C., Magrini L., Pappalardo C., Boselli A., Bendo G. J., 2012, A&A, 542, A32
Davies J. I. et al., 2010, A&A, 518, L48
Dehnen W., Binney J., 1998, MNRAS, 294, 429
Della Valle M. et al., 2006, Nature, 444, 1050
Dobbs C. L. et al., 2013, in Beuther H., Klessen R. S., Dullemond C. P., Henning T., eds, Protostars and Planets VI. Univ. Arizona, Tucson, in press
Dopcke G., Glover S. C. O., Clark P. C., Klessen R. S., 2011, ApJ, 729, L3
Dwek E., Scalo J. M., 1980, ApJ, 239, 193
Efstathiou G., 2000, MNRAS, 317, 697
Fraser M. et al., 2011, MNRAS, 417, 1417
Frebel A., Norris J. E., 2013, Planets, Stars and Stellar Systems. Springer-Verlag, Berlin
Frebel A. et al., 2005, Nature, 434, 871
Frebel A., Johnson J. L., Bromm V., 2007, MNRAS, 380, L40
Fu J. et al., 2013, MNRAS, 434, 1531
Gal-Yam A. et al., 2011, ApJ, 736, 159
Galametz M., Madden S. C., Galliano F., Hony S., Bendo G. J., Sauvage M., 2011, A&A, 532, A56 (G11)
Ganguly R., Sembach K. R., Todd T. M., Savage B. D., 2005, ApJ, 157, 251
Gnedin N. Y., 2000, ApJ, 542, 535
Greif T. H., Bromm V., Clark P. C., Glover S. C. O., Smith R. J., Klessen R. S., Yoshida N., Springel V., 2012, MNRAS, 424, 399
Gunn J. E. et al., 2006, AJ, 131, 2332
Heger A., Woosley S. E., 2002, ApJ, 567, 532
Heger A., Woosley S. E., 2010, ApJ, 724, 341
Hirano S., Hosokawa T., Yoshida N., Umeda H., Omukai K., Chiaki G., Yorke H. W., 2014, ApJ, 781, 60
Hoeft M., Yepes G., Gottlöber S., Springel V., 2006, MNRAS, 371, 401
Horiuchi S., Beacom J. F., Kochanek C. S., Prieto J. L., Stanek K. Z., Thompson T. A., 2011, ApJ, 738, 154
Hosokawa T., Omukai K., 2009, ApJ, 703, 1810
Hosokawa T., Omukai K., Yoshida N., Yorke H. W., 2011, Science, 334, 6060
Jenkins E. B., 2009, ApJ, 700, 1299
Joggerst C. C., Woosley S. E., Heger A., 2009, ApJ, 693, 1780
Jones A. P., Tielens A. G. G. M., Hollenbach D. J., 1996, ApJ, 469, 740
Karlsson T., 2006, ApJ, 2006, 641, L41
Karlsson T., Bromm V., Bland-Hawthorn J., 2013, Rev. Mod. Phys., 85, 809
Keller S. C. et al., 2014, Nature, 506, 463
Kennicutt R. C. et al., 2011, PASP, 123, 1347
Klessen R. S., Glover S. C. O., Clark P. C., 2012, MNRAS, 421, 3217
Klypin A. A., Zhao H., Somerville R. S., 2002, ApJ, 573, 597
Kobayashi C., Tominaga N., Nomoto K., 2011, ApJ, 730, L14
Komiya Y., 2011, ApJ, 736, 73
Komiya Y., Habe A., Suda T., Fujimoto M. Y., 2009, ApJ, 696, L79
Komiya Y., Habe A., Suda T., Fujimoto Y. M., 2010, ApJ, 717, 542
Kuo T.-M., Hirashita H., Zafar T., 2013, MNRAS, 436, 1238
Larson R. B., 1998, MNRAS, 301, 569
Lee Y. S., Suda T., Beers T. C., Lucatello S., 2013, ApJ, 788, 131
Limongi M., Chieffi A., 2012, ApJS, 199, 38
Lucatello S., Tsangarides S., Beers T. C., Carretta E., Gratton R. G., Ryan S. G., 2005, ApJ, 625, 825
McKee C., 1989, in Allamandola L. J., Tielens A. G. G. M., eds, Proc. IAU Symp. 135, Interstellar Dust. Kluwer, Dordrecht, p. 431

Madden S. C. et al., 2013, PASP, 125, 600
Marassi S., Schneider R., Limongi M., Chieffi A., 2014, ApJ, 794, 100
Masseron T., Johnson J. A., Plez B., van Eck S., Primas F., Goriely S., Jorissen A., 2010, A&A, 509, 93
Noh Y., McQuinn M., 2014, MNRAS, 444, 503
Norris J. E., Christlieb N., Korn A. J., Eriksson K., Bessell M. S., Beers T. C., Wisotzki L., Reimers D., 2007, ApJ, 670, 774
Norris J. E. et al., 2013, ApJ, 762, 28
Nozawa T., Kozasa T., Habe A., 2006, ApJ, 648, 435
Okamoto T., Gao L., Theuns T., 2008, MNRAS, 390, 920
Omukai K., 2000, ApJ, 534, 809
Omukai K., Tsuribe T., Schneider R., Ferrara A., 2005, ApJ, 626, 627
Omukai K., Hosokawa T., Yoshida N., 2010, ApJ, 722, 1793
Pastorello A. et al., 2004, MNRAS, 347, 74
Pastorello A. et al., 2006, MNRAS, 370, 1752
Planck Collaboration XXV, 2011, A&A 536, A25
Planck Collaboration XVI, 2014, A&A, (doi:10.1051/0004-6361/201321591)
Podio L., Bacciotti F., Nisini B., Eisloffel J., Massi F., Giannini T., Ray T. P., 2006, A&A, 456, 189
Powell L. C., Slyz A., Devriendt J., 2011, MNRAS, 414, 3671
Press W. H., Schechter P., 1974, ApJ, 187, 425
Raiteri C. M., Villata M., Navarro J. F., 1996, A&A, 105, 315
Rémy-Ruyer A., Madden S. C., Galliano F., Galametz M., Takeuchi T. T., Asano R. S., Zhukovska S., Lebouteiller V., 2014, A&A, 563, A31
Safranek-Shrader C., Milosavljević M., Bromm V., 2014, MNRAS, 438, 1669
Salvadori S., Ferrara A., 2009, MNRAS, 395, L6
Salvadori S., Ferrara A., 2012, MNRAS, 421, L29
Salvadori S., Schneider R., Ferrara A., 2007, MNRAS, 381, 647
Salvadori S., Ferrara A., Schneider S., 2008, MNRAS, 386, 348
Salvadori S., Ferrara A., Schneider S., Scannapieco E., Kawata D., 2010, MNRAS, 401, L5
Salvadori S., Tolstoy E., Ferrara A., Zaroubi S., 2014, MNRAS, 437, L26
Schaerer D., 2002, A&A, 382, 28
Schneider R., Ferrara A., Natarajan P., Omukai K., 2002, ApJ, 571, 30
Schneider R., Ferrara A., Salvaterra R., 2004, MNRAS, 351, 1379
Schneider R., Omukai K., Inoue A. K., Ferrara A., 2006, MNRAS, 369, 1437
Schneider R., Omukai K., Bianchi S., Valiante R., 2012a, MNRAS, 419, 1566
Schneider R., Omukai K., Limongi M., Ferrara A., Salvaterra R., Chieffi A., Bianchi S., 2012b, MNRAS, 423, L60
Schneider R., Valiante R., Ventura P., dell Agli F., Di Criscienzo M., Hirashita H., Kemper F., 2014, MNRAS, 442, 1440
Schörck T. et al., 2009, A&A, 507, 817
Slavin J. D., 2009, Space Sci. Rev., 143, 311
Spite M., Caffau E., Bonifacio P., Spite F., Ludwig H.-G., Plez B., Christlieb N., 2013, A&A, 552, A107
Stahler W. S., Palla F., 2004, The Formation of Stars. Wiley, New York
Suda T., Aikawa M., Machida M. N., Fujimoto M. Y., 2004, ApJ, 611, 476
Tielens A. G. G. G., 2005, The Physics and Chemistry of the Interstellar Medium. Cambridge Univ. Press, Cambridge
Tolstoy E., Hill V., Tosi M., 2009, ARA&A, 47, 371
Tominaga N., Umeda H., Nomoto K., 2007, ApJ, 660, 516
Tsuribe T., Omukai K., 2006, ApJ, 642, L61
Tsuribe T., Omukai K., 2008, ApJ, 676, L45
Tumlinson J., 2006, ApJ, 641, 1
Tumlinson J., 2007, ApJ, 664, L63
Turatto M. et al., 1998, ApJ, 498, L129
Turk M. J., Oishi J. S., Abel T., Bryan G. L., 2012, ApJ, 745, 154
Umeda H., Nomoto K., 2002, ApJ, 565, 385
Umeda H., Nomoto K., 2003, Nature, 422, 871
Valiante R., Schneider R., 2014, in Andersen A., Baes M., Gomez H., Kemper C., Watson D., eds, Proceedings of Science, The Life Cycle of Dust in the Universe: Observations, Theory, and Laboratory Experiments - LCDU 2013, Taipei, Taiwan
Valiante R., Schneider R., Bianchi S., Andersen A. C., 2009, MNRAS, 397, 1661
Valiante R., Schneider R., Salvadori S., Bianchi S., 2011, MNRAS, 416, 1916
Valiante R., Schneider R., Salvadori S., Gallerani S., 2014, MNRAS, 444, 2442
Van den Hoek L. B., Groenewegen M. A. T., 1997, A&A, 123, 305
Welty D. E., Jenkins E. B., Raymond J. C., Mallouris C., York D. G., 2002, ApJ, 579, 304
Wisotzki L., Christlieb N., Bade N., Beckmann V., Köhler T., Vanelle C., Reimers D., 2000, A&A, 358, 77
Woosley S. E., Weaver T. A., 1995, ApJ, 101, 181
Yanny B. et al., 2009, AJ, 137, 4377
Yong D. et al., 2013a, ApJ, 762, 26
Yong D. et al., 2013b, ApJ, 762, 27
York D. G. et al., 2000, AJ, 120, 1579
Zafar T., Watson D., 2013, A&A, 560, A26
Zhukovska S., 2014, A&A, 562, A76
Zhukovska S., Gail H. P., Trieloff M., 2008, A&A, 479, 453

This paper has been typeset from a TEX/LATEX file prepared by the author.